Author's Accepted Manuscript

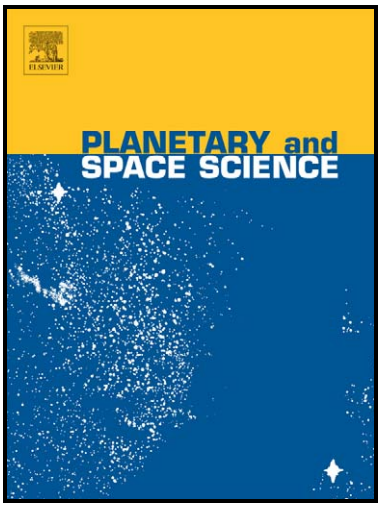

www.elsevier.com/locate/pss

The mercury imaging X-ray spectrometer (MIXS) on BepiColombo

G.W. Fraser, J.D. Carpenter, D.A. Rothery, J.F. Pearson, A. Martindale, J. Huovelin, J. Treis, M. Anand, M. Anttila, M. Ashcroft, J. Benkoff, P. Bland, A. Bowyer, A. Bradley, J. Bridges, C. Brown, C. Bulloch, E.J. Bunce, U. Christensen, M. Evans, R. Fairbend, M. Feasey, F. Giannini, S. Hermann, M. Hesse, M. Hilchenbach, T. Jorden, K. Joy, M. Kaipiainen, I. Kitchingman, P. Lechner, G. Lutz, A. Malkki, K. Muinonen, J. Näränen, P. Portin, M. Prydderch, J. San Juan, E. Sclater, E. Schyns, T.J. Stevenson, L. Strüder, M. Syrjasuo, D. Talboys, P. Thomas, C. Whitford, S. Whitehead

PII: S0032-0633(09)00148-2
DOI: doi:10.1016/j.pss.2009.05.004
Reference: PSS 2672

To appear in: *Planetary and Space Science*

Received date: 11 February 2008
Revised date: 2 April 2009
Accepted date: 7 May 2009

Cite this article as: G.W. Fraser, J.D. Carpenter, D.A. Rothery, J.F. Pearson, A. Martindale, J. Huovelin, J. Treis, M. Anand, M. Anttila, M. Ashcroft, J. Benkoff, P. Bland, A. Bowyer, A. Bradley, J. Bridges, C. Brown, C. Bulloch, E.J. Bunce, U. Christensen, M. Evans, R. Fairbend, M. Feasey, F. Giannini, S. Hermann, M. Hesse, M. Hilchenbach, T. Jorden, K. Joy, M. Kaipiainen, I. Kitchingman, P. Lechner, G. Lutz, A. Malkki, K. Muinonen, J. Näränen, P. Portin, M. Prydderch, J. San Juan, E. Sclater, E. Schyns, T.J. Stevenson, L. Strüder, M. Syrjasuo, D. Talboys, P. Thomas, C. Whitford and S. Whitehead, The mercury imaging X-ray spectrometer (MIXS) on BepiColombo, *Planetary and Space Science*, doi:10.1016/j.pss.2009.05.004

The Mercury Imaging X-ray Spectrometer (MIXS) on BepiColombo

G.W. Fraser[1*], J.D. Carpenter[1], D.A. Rothery[2], J.F. Pearson[1], A. Martindale[1], J. Huovelin[3], J. Treis[4,5], M. Anand[2], M. Anttila[6], M. Ashcroft[7], J. Benkoff[8], Bland, P.[9], A. Bowyer[7], A. Bradley[7], J. Bridges[1], C. Brown[1], C. Bulloch[7], E.J. Bunce[1], U. Christensen[4], M. Evans[1], R. Fairbend[10], M. Feasey[7], F. Giannini[8], S. Hermann[11,5], M. Hesse[12], M. Hilchenbach[4], T. Jorden[13], K. Joy[14,15], M. Kaipiainen[16], I. Kitchingman[7], P. Lechner[17,5], G. Lutz[17,5], A. Malkki[18], K. Muinonen[3], J. Näränen[3], P. Portin[19], M. Prydderch[15], J. San Juan[20], E. Sclater[7], E. Schyns[10], T.J. Stevenson[1], L. Strüder[11,5], M. Syrjasuo[18], D. Talboys[1], P. Thomas[7], C. Whitford[1], S. Whitehead[7].

[1]Space Research Centre, Department of Physics and Astronomy, University of Leicester, University Road, Leicester, LE1 7RH, UK

[2]Department of Earth and Environmental Sciences, The Open University, Walton Hall, Milton Keynes, MK7 6AA, Milton Keynes, UK

[3]University of Helsinki Observatory, University of Helsinki, 00014 Helsinki, Finland

[4]Max Planck Institute for Solar System Research, Max-Planck-Str. 2, 37191 Katlenburg-Lindau, Germany

[5] Max Planck Institute Halbleiterlabor, Otto-Hahn-Ring 6, 81739 Munich, Germany

[6]Space Systems Finland Ltd., Kappelitie 6 B, 02200 Espoo, Finland

[7]Magna Parva Ltd, Loughborough Innovation Centre, Epinal Way, Loughborough, Leicestershire, LE11 3EH

22 [8]ESA/ESTEC, Keplerlaan 1, Postbus 299, 2200 AG, Noordwijk, The Netherlands.

23 [9] Impacts and Astromaterials Research Centre, Department of Earth Science and
24 Engineering, Imperial College London, South Kensington Campus, London SW7 2AZ,
25 UK.

26 [10]Photonis SAS, Av. Roger Roncier BP520, 19106 Brive cedex, France

27 [11]Max Planck Institute für Extraterrestrische Physik, Giessenbachstraße, 85748 Garching,
28 Germany

29 [12] Centro de Astrobiología (CSIC/INTA), Instituto Nacional de Técnica Aeroespacial,
30 Ctra de Torrejón a Ajalvir, km 4, 28850 Torrejón de Ardoz, Madrid, Spain

31 [13]EADS Astrium Ltd, Gunnels Wood Road, Stevenage, SG1 2AS, UK

32 [14]UCL/Birkbeck Research School of Earth Sciences, UCL, Gower Street, London, WC1E
33 6BT, UK.

34 [15]Rutherford Appleton Laboratory, Harwell Science and Innovation Campus,
35 Didcot, Oxfordshire, OX11 0QX, UK

36 [16]Oxford Instruments Analytical Oy, PO Box 85 (Nihtisillankuja 5), Fin-02361 Espoo,
37 Finland

38 [17]PNSensor GmbH, Römerstrasse 28, 80803, Munich, Germany

39 [18]Finnish Meteorological Institute, Erik Palménin Aukio, FI-00560, Helsinki, Finland

40 [19]Patria Aviation OY, Naulakatu 3, FI-33100, Tampere, Finland

41 [20]LIDAX, Ax. Cristóbal Colón 16, 28850 Torrejon de Ardoz, Madrid, Spain

42

43

44 *e-mail: gwf@star.le.ac.uk

45 Telephone: +44 (0) 116 252 3542

46 Fax: +44 (0) 116 252 2464

47

Abstract

The Mercury Imaging X-ray Spectrometer (MIXS) on the BepiColombo Mercury Planetary Orbiter (MPO), will measure fluorescent X-ray emission from the surface of Mercury in the energy range 0.5 – 7.5 keV, which is induced by incident solar X-rays and solar wind electrons and protons. These X-rays will reveal the elemental composition of the surface of Mercury and aid the determination of the planet's evolution.

MIXS is a two component instrument. A collimated channel (MIXS-C) provides measurements on scales of 70-270 km, sufficient to separate the major Mercurian terrains. A second channel (MIXS-T) is the first imaging X-ray telescope for planetary remote sensing and will make measurements on spatial scales of less than 10 km for major elements during solar flares, sufficient to isolate surface landforms, such as craters and their internal structures. The spatial resolution achieved by MIXS-T is made possible by novel, low mass microchannel plate X-ray optics, in a Wolter type I optical geometry.

MIXS measurements of surface elemental composition will help determine rock types, the evolution of the surface and ultimately a probable formation process for the planet. In this paper we present MIXS and its predicted performance at Mercury as well as discussing the role that MIXS measurements will play in answering the major questions about Mercury.

Keywords

Mercury; BepiColombo; X-ray fluorescence; composition; instrumentation

1 Introduction

The innermost planet, Mercury represents an end member of the solar system in terms of size, metal-to-silicate ratio and probably conditions of formation. Knowledge of Mercury's history and formation is therefore essential to understand the formation and evolution of the inner solar system as a whole. Mercury is also the least explored of all the planets. Until recently, three brief flybys by Mariner 10 in 1974 and 1975 provided the only detailed measurements of the planet. At the time of writing (January 2008) the first data is being returned from NASA's MESSENGER mission to Mercury, which flew by the planet on 14th January 2008. Following additional flybys in October 2008 and September 2009, MESSENGER will ultimately go into orbit around Mercury in 2011. These data, coupled with ground based measurements, have provided a picture of an anomalously dense, airless and heavily cratered world which superficially resembles the Moon. Mercury's very large core and an apparent paucity of iron at the surface (estimated, on the basis of ground-based spectroscopy, at less than 3 wt % FeO) are only two of the more striking differences between the two bodies (Strom and Sprague, 2003; Solomon, 2003).

The major unanswered questions at Mercury may be divided into two categories

Primary questions:

- From what material did Mercury form, and how?
- How and when did Mercury become internally differentiated?

- Is there both primary and secondary crust on Mercury (as defined by Taylor, 1989)?
- Why does Mercury have a dipole magnetic field?

Secondary questions:

- What is the history of crustal evolution on Mercury?
- What is the crustal composition and how does it vary (i) across the surface, (ii) with depth?
- How are the surface and exosphere related?
- How do the surface and magnetosphere interact?
- Does Mercury have a molten core?
- What are the deposits observed in craters near to the poles?

The Mercury Imaging X-ray Spectrometer (MIXS) on BepiColombo Mercury Planetary Orbiter (MPO) will measure fluorescent X-rays from the surface of Mercury. Fluorescent X-rays reveal the elemental composition of the surface to depths of a few micrometres for low atomic number elements such as magnesium and for the L-shell emission lines of heavier elements. For the harder, K-shell emission lines of heavier elements, measurements of the fluorescent X-rays probes a deeper layer of the planetary surface (of order tens of microns). Measurement of the composition of the regolith in this way is a tool for determining the geological history and ultimately the formation mechanisms for the planet. X-ray spectroscopy is complementary to measurements at optical and infrared wavelengths which indicate chemical bonding and mineralogy, and to gamma ray and

115 neutron measurements which provide low spatial resolution measurements of certain
116 elements at depths of approximately 10 cm. In this paper we describe the production of
117 X-rays on Mercury's surface, the MIXS instrument and its capabilities and the expected
118 contribution that measurements by MIXS will make towards answering the major
119 questions about Mercury.

120 **2 X-ray remote sensing**

121 X-ray fluorescence has been used for remote sensing on Apollo 15 and 16 at the Moon
122 (Adler et al., 1973), on the Near Earth Asteroid Rendezvous (NEAR Shoemaker) mission
123 to asteroid 433 Eros (Trombka et al., 2000), on the Hayabusa mission to asteroid 25143
124 Itokawa (Okada et al., 2006) and on the SMART-1 mission to the Moon (Grande et al.,
125 2003). The Chandrayaan 1 and Kaguya (Selene) missions to the Moon also carry X-ray
126 spectrometers (Grande et al., 2008 and Shirai et al. 2008). The X-ray spectrometer on
127 MESSENGER (Leary et al., 2007) is derived from those on Apollo and NEAR
128 Shoemaker and uses collimated gas proportional counters as the detectors of X-rays
129 (Schlemm et al., 2007). The instruments on SMART-1 and Chandrayaan 1 were based on
130 silicon Swept Charge Device (SCD) detectors (Lowe et al., 2001), while those on
131 Hayabusa and Kaguya use silicon Charge Coupled Device (CCD) detectors. The
132 detectors on MESSENGER have an energy resolution of ~ 880 eV Full Width at Half
133 Maximum (FWHM) at 5.9 keV (Schlemm et al., 2007) and, as was the case for Apollo
134 before them, the separation of the K shell emission lines from Mg (1.25 keV), Al (1.49
135 keV) and Si (1.74 keV) is not possible. Instead, three separate detectors are employed
136 with thin Be windows, two of which bear an additional thin Mg or Al filter. The
137 differential X-ray attenuation of the three counters is then used to infer the relative

138 heights of the three peaks and produce elemental abundance ratios. The MESSENGER
139 X-ray spectrometer's field of view (FOV) is selected by a 12º collimator which, when
140 coupled with the highly elliptical orbit, results in a surface footprint of approximately
141 3000 km at apoherm (15193 km), and 40 km at periherm (200 km), the later resolution
142 being available for approximately 15 minutes in each 12 hour orbit. (Schlemm et al.,
143 2007).
144
145 MIXS differs radically from previous X-ray instruments for planetary remote sensing,
146 offering unprecedented spectral and spatial resolutions. MIXS has two complementary
147 instrument channels shown in Figure 1; MIXS-C (collimator) and MIXS-T (telescope).
148 MIXS-C has a 10.4° Field Of View (FOV), which defines its angular resolution, and is
149 optimised to provide the largest X-ray throughput at all energies and for all solar states.
150 The MIXS-C FOV results in a surface pixel size of 70 km at periherm (400 km orbital
151 altitude) and 270 km at apoherm (1500 km orbital altitude). MIXS-T is an imaging X-ray
152 telescope with a 1.1° FOV and has an angular resolution better than 9 arc minutes, which
153 may be used to full effect during solar flares when the incident (and thence the
154 fluorescent) X-ray flux is highest. MIXS-T's angular resolution is sufficient to provide a
155 spatial resolution better than 1 km at periherm and 4 km at apoherm. Together these two
156 channels ensure comprehensive measurements of the compositions of the major terrains
157 and, where solar conditions allow, the compositions of landform elements such as crater
158 peaks at spatial scales less than 10 km.

3 The relationship between Mercury's composition and its formation

Mercury has an extraordinarily large uncompressed density (5.3 g cm^{-3} compared with 4.0 g cm^{-3} for Earth), which is incompatible with models of formation by equilibrium condensation (Cameron et al., 1988) and indicates that Mercury's metallic mass fraction is at least twice that of the other terrestrial planets (Solomon, 2003). A large iron-rich core is postulated, which occupies about 42% of the planet's volume and 75% of the radius and there is evidence that it is at least partly molten (Margot et al., 2007).

Several models have been proposed to explain the relative sizes of Mercury's core and its silicate fraction (mantle plus crust). These models fall into three basic categories: selective accretion, post accretion vaporisation and massive impact.

In the first of these models, the oxidation gradient during solar nebula condensation, aided by gravitational and drag forces, resulted in an enrichment of metallic iron compared with other terrestrial planets (Weidenschilling, 1978). In the second, intense solar radiation in the early Solar System led to the vaporisation and loss of silicates from Mercury's exterior after the planet had formed (Cameron, 1985), or possibly from the differentiated exteriors of planetary embryos before they collided to form Mercury. In the latter model, a giant impact stripped Mercury of much of its rocky exterior (Benz et al., 1988, 2007). A range of credible compositions for Mercury's mantle plus crust, which result from the proposed models, is tabulated in Table 1.

4 Crust formation on Mercury and effects on surface elemental composition

The measured abundance of elements on Mercury's surface cannot, however, be representative of the bulk silicate fraction (mantle plus crust). The crust, whether "primary" or "secondary" (Taylor, 1989) or both, must be chemically differentiated from the mantle by processes dependent on its emplacement mechanisms. Space weathering may further change the surface elemental abundances, so none of the models in Table 1 is likely to correspond to the detected surface composition.

Primary crust is the oldest surviving crust, and would have derived from a magma ocean (a highly-likely eventuality in any planetary growth scenario involving embryo-embryo collision and/or a final 'giant impact'). Primary crust would be comprised of minerals that grew by fractional crystallisation from a magma ocean melt of mantle (bulk silicate) composition and floated to the surface. This crustal material would be analogous to, and enriched in certain elements in ways comparable to, the anorthosites of the lunar highlands which are enriched in Al and Ca relative to the mantle's bulk composition. Na may be enriched to detectable concentrations in primary crust, although Na concentrations are less than 1.5% in lunar anorthosites, and both Fe and Mg would be depleted. The final crystallisation products of a magma ocean would be expected to have enrichments in the incompatible elements such as K and the rare Earth elements, analogous to the KREEP (Potassium, Rare Earth Elements and Phosphorus) component identified on the Moon.

202 Secondary crust results from partial melting in the mantle and will have been emplaced
203 volcanically. Secondary crust will tend to be enriched in Fe (Robinson and Taylor, 2001)
204 but depleted in Mg relative to the bulk composition. Secondary crust will also have a
205 greater abundance of Al, Ca and Na than the mantle (but less than primary crust), and
206 will be richer in K, Ti and Cr than any other major silicate component of the planet.
207 Silicon abundance will probably be less in secondary crust than in primary crust, but the
208 fractional change in Si abundance between crustal types will be small compared to that
209 for other elements, depending on the extent of partial melting. Material erupted after
210 storage and differentiation in large-volume basaltic magma chambers will be lower in Fe
211 and Ti but richer in alkalis than in directly-erupted basalts (Jeanloz et al., 1995).
212
213 Extensive tracts of exposed primary crust on Mercury have yet to be identified. The
214 planet's surface may prove to be largely secondary crust, but it will be important to
215 identify and characterise any exposures of primary crust that have survived resurfacing
216 (or have been re-exposed through tectonism or impact cratering). With the understanding
217 that the Moon is not necessarily a close analogue for Mercury, we present data in Table 2
218 to indicate the sorts of variation in crustal composition at Mercury that an instrument
219 such as MIXS needs to be able to measure. The diagnostic significance of the elements
220 shown in Table 2 is discussed further in Section 5 of this paper.
221 Long-term exposure to meteorite impacts and energetic particles may further alter surface
222 elemental abundances, by processes often described as 'space weathering'. One
223 consequence of this may be the reduction of Fe bonded to oxygen within silicates to
224 metallic 'nanophase iron', alternatively known as submicroscopic metallic iron (SMFe)

225 particles (Blewett et al., 2002). Infrared – ultraviolet spectroscopy is not sensitive to
226 metallic Fe and so X-ray spectroscopy provides the only mechanism for detection of Fe
227 in SMFes. These provide a possible explanation for the apparent deficiency of Fe in
228 surface minerals. MIXS is therefore a crucial complement to the optical and infrared
229 spectrometers on BepiColombo (Simbio-Sys (this issue) and MERTIS (this issue)).
230
231 Determination of Mercury's bulk silicate composition on the basis of surface
232 measurements requires the identification and understanding of the history of crust
233 formation and of the subsequent surface processes. This requires a combination of
234 elemental analysis by X-ray, neutron and gamma ray spectroscopy, visual interpretation
235 of geological features on high-resolution optical images, and infrared – ultraviolet
236 spectroscopy to infer mineralogy.
237

238 **5 The importance of different elements at Mercury**

239 The following arguments describe the diagnostic significance of various elements whose
240 fluorescent X-ray emission is within the energy range detectable by MIXS.
241
242 **Si**: Expected in a narrow range, 19-25% (15–33% in some lunar specimens). Si as a
243 stand-alone element is unlikely to allow determination of mechanisms for Mercury's
244 formation or the evolution of the surface but is useful, not least as a reference to which
245 other elements may be compared.
246

247 **Ti**: Between 1% and 8% in lunar and terrestrial basalts. Abundances greater than 3% on
248 Mercury would indicate sufficient oxygen fugacity to form Ti-oxides (as opposed to Ti
249 merely substituting for other cations within silicates). A Ti abundance of approximately
250 0.1% or less in lavas would support an enstatite chondrite model for Mercury's
251 composition (Taylor and Scott, 2004).
252
253 **Al**: By analogy with the Moon, expected to be abundant in primary crust (~18%), but
254 between 4% and 10% in basalts. Distinguishing between, for example, 18% and 10% Al
255 content would allow the separation of primary and secondary crust.
256
257 **Fe**: The confirmation or otherwise of a low Fe abundance in Mercury's crust is of key
258 importance. Fe abundance is expected to be less than 2% in primary crust, but could be at
259 least 4% in secondary crust. Fe concentration of less than 0.3% would support an
260 enstatite chondrite origin for Mercury's composition (Taylor and Scott, 2004).
261
262 **Mg**: Should be rare in primary crust (less than 2%), but abundant (4-12%) in secondary
263 crust unless the outer part of Mercury has been stripped to reveal inner mantle Mg-rich
264 cumulate. A Magnesium concentration less than 7% would support a refractory-volatile
265 mixture model of Mercury, whereas more than 10% in lavas would support other models
266 (Taylor & Scott, 2004).
267
268 **Na**: Possibly as much as 1% in primary crust and expected to be less abundant in most
269 basalts, although some terrestrial basalts contain more than 1% Na. Detection of Na

would place constraints on the volatile budget within Mercury. The liberation of Na into the exosphere from surface material may occur through interplanetary dust impacts, large impacts and the subsequent exposure of fresh regolith, thermal desorption and evaporation, recycling processes from cold craters and ion sputtering.

Ca: By analogy with the Moon, Ca should be abundant in primary crust (18-20%) but rarer in secondary crust (8-14%). A Ca concentration of less than 9% in units recognised as lava would support an enstatite chondrite model of Mercury's composition (Taylor and Scott, 2004). Like Na, Ca is also a constituent of Mercury's exosphere.

P: Reaches concentrations of about 0.1% in lunar mare basalts and double that in the petrologically significant KREEP basalts of the lunar highlands. P and Ti have similar partitioning behaviour during partial melting, and the Ti/P ratio in chondrites is about 1. Thus, a Ti/P of order 10 in volcanic terrains on Mercury would indicate previous scavenging of P into the core and thus provide compelling confirmation of Mercury core formation prior to volcanism.

Mn: Reaches about 0.3% in lunar mare basalts but is much less abundant in primary crust. If detectable on Mercury, it would be expected in secondary crust only.

K: Effectively absent in lunar primary crust, but up to as much as 1% in some kinds of lunar secondary crust and higher in some impact melts. If detected on Mercury,

potassium may be used in conjunction with other elements to constrain basalt petrogenesis. K is also a major component of the exosphere.

S: Fe sulphides could provide the sulphur observed in the exosphere and inferred from radar backscatter from Mercury's poles (Sprague et al., 1995, 1996). S concentration is probably much less than 1% except possibly in areas of high-radar reflectivity in polar craters, where sulphur is an alternative candidate to water ice for the material making up the reflective layer. X-ray emission from S inside polar craters would have to be induced by incident electrons (and/or protons) in the absence of direct illumination by the Sun.

Cr: Averages 500 – 600 ppm in the lunar crust. Cr of order 1% in rocks identified as lava would support a refractory-volatile mixture model of Mercury, whereas 0.1% would support other models (Taylor and Scott, 2004).

Ni: Present in abundances less than 400 ppm in the lunar crust, and potentially diagnostic in conjunction with Cr. On the Moon the Cr:Ni abundance ratio has been used to constrain formation models (Taylor, 1975).

O: It is conventionally assumed that in silicate rocks cations (all elements in Table 2 apart from S) are oxidised. O is therefore likely to be about 44-46% in surface materials. A significant departure from this abundance would call into question the whole mineralogy of Mercury's crust.

315 In addition, the acquisition of volatile elements will indicate whether Mercury conforms
316 to the approximate trend of increasing depletion with decreasing heliocentric distance,
317 defined by C-type asteroids in the outer belt, to S-type, to E-type in the inner belt, to
318 Mars, to Earth (Bland and Benedix, 2006). Determining volatile abundances will also
319 allow constraints to be placed on volatile depletion during a putative giant impact.

320 **6 Solar X-ray induced fluorescence from Mercury's surface**

321 The primary mechanism for producing X-ray fluorescence from airless planetary bodies
322 in the inner solar system, within approximately 3 AU of the Sun (Adler and Trombka,
323 1970; Adler et al., 1972), is excitation by solar coronal X-rays, although fluorescence can
324 also be induced through bombardment by charged particles. Solar X-ray induced X-ray
325 fluorescence spectroscopy as an observational technique is therefore limited to the Moon,
326 Mercury, asteroids and comets in the inner solar system.
327
328 The intensity of X-ray fluorescence from the various elements on a planet's surface
329 depends on the energy and intensity of incident solar X-rays, but solar X-ray intensity can
330 vary by several orders of magnitude and can be highly variable on time scales of minutes.
331 It is therefore essential that measurements of planetary fluorescent X-ray emission are
332 accompanied by simultaneous measurements of the solar X-ray spectrum. On
333 BepiColombo, solar X-rays will be measured by the Solar Intensity X-ray and Particle
334 Spectrometer, SIXS (Huovelin et al., this volume), which also characterises the particle
335 environment local to the spacecraft. These measurements by SIXS allow normalisation of
336 fluorescence measurements from different orbits allowing the correction of data in order
337 to give a self-consistent picture of the surface.

Figure 2 shows the solar X-ray flux as a function of energy for various solar flare states measured at 1 AU by the X-ray Solar Monitor (XSM) on SMART 1 (Huovelin et al., 2002). Solar flare states are defined according to the total energy output of the sun measured in the wavelength range 1-8 Å, as measured by the NOAA's GOES spacecraft, in orbit around the Earth. Flare states are designated as : solar quiet (A1 flare), B, C, M or X on a scale where an X1 flare is 10 times an M1 flare is 10 times a C1 flare etc. The largest solar flare to date, in November 2003, is believed to have peaked at around X40 (Brodrick et al., 2005). Also shown in Figure 2 are polynomial approximations to solar spectra taken from Truscott et al. (2000). The polynomial approximation to the solar quiet spectrum below 4 keV is smoothed and extrapolated from the 0.3-2.7 keV spectrum reported by Fichtel and Trombka (1997) who in turn used earlier (semi-empirical) work by Tucker and Koren (1971) based on observations from Apollo 15. Above 4 keV, data from Clark et al. (1997) are added. Line emissions were not included in these spectra because the hotter the solar coronal plasma (i.e. the more active the Sun), the more the total continuum emission will dominate. Nevertheless, Tucker and Koren (1971) include more than 450 lines in their solar coronal model; these lines will be included in future MIXS calculations. The detection of lines in the measured solar spectra of Figure 2 is limited by the spectral resolution of the XSM detector. The Fe-Kα line is resolved in the M-flare XSM data at 6.6 keV, shifted from 6.4 keV for cold iron because of the increased ionization state for Fe in the solar corona.

The solar spectrum will be scattered from the planetary surface as well as initiating fluorescence. However, the energy resolution of the MIXS instrument will allow it to

detect the shift in energy between elastically and inelastically scattered X-ray line emission. The XSM "C1 flare" data shown in Figure 2 was recorded during a C2 flare event and reduced by a factor of 2. The divergence of the XSM solar quiet data from its representative polynomial, above 4 keV, is probably due to the inclusion of the diffuse X-ray background (DXB) and galactic X-ray background within the 52° XSM field view. The predicted contribution to the measured flux due to the DXB (whose intensity is given by Zombeck, 2007) is also shown in Figure 2.

BepiColombo will arrive at Mercury shortly after solar minimum in August 2019, with a nominal mission duration of 1 year, extensible to 2 years. Representing the years of operation at Mercury with the corresponding years, two solar cycles earlier, around solar minimum in 1997, we can estimate the fractions of a year for which the Sun is expected in various flare states in 2019 and 2020 (Huovelin et al. (this volume)).

If E is the X-ray energy and the incident intensity of parallel solar X-rays on Mercury's surface is $I_0(E)$ (photons cm^{-2} s^{-1}) then the intensity of fluorescence from a given X-ray line (photons cm^{-2} s^{-1} steradian^{-1}) can be determined in terms of fundamental physical parameters by the relationship shown in Equation 1, adapted from Clark and Trombka (1997).

$$I_{line} = \frac{1}{4\pi} w_i g C_i \left(\frac{r-1}{r}\right) \int_{E_{abs}}^{\infty} I_0(E) \rho \cos\theta \frac{\left(\frac{\mu(E)_i}{\rho_i}\right)}{\mu(E) + \mu(E_{line}) \frac{\cos\theta}{\cos\phi}} dE \qquad (1)$$

where w_i is the fluorescence yield of a given emission series (K,L etc.), g is the weight fraction of a given line within a series (α, β etc.), C_i is the mass fraction of a given element, r is the jump ratio at the absorption edge of interest, ρ is the bulk density of the surface material, ρ_i is the partial density of the element of interest, θ is the angle of incidence of the incident solar X-rays, measured from the surface normal and ϕ is the viewing angle measured from the surface normal. $\mu(E)$ is the mass absorption coefficient of the bulk material and $\mu(E)_i$ is the linear absorption coefficient for the element of interest. E_{line} is the energy of the elemental emission line of interest.

Equation 1 assumes a perfectly smooth and homogeneous planar surface; no allowance is made for effects due to the real properties of the planetary regolith, including surface roughness and packing density. Also unaccounted for in Equation 1 are shadowing effects due to large scale topography. Energy independent effects of the regolith and topography (e.g. shadowing) may be removed by the use of elemental abundance ratios (e.g. Mg:Si, Al:Si) instead of absolute abundances, however the use of ratios cannot remove any effects for which there is an energy dependency, and it has been shown in preliminary measurements that for large values of θ and ϕ the measured ratios of elemental line intensities varies as a function of surface roughness by 10% - 20% (Näränen et al., 2007,Okada et.al, 2004). Work is continuing at the University of Leicester, the University of Helsinki and Birkbeck College to quantify the effects of regolith properties on line intensities, in order to provide a more complete interpretation of X-ray fluorescence data from planetary surfaces.

To indicate the fluorescence emission spectrum expected from Mercury's surface, line emissions calculated from Equation 1 are shown in Figure 3. Solar input spectra for the simulation are the polynomials shown in Figure 2, scaled to an average Mercury-Sun separation of 0.39 AU. Also shown in Figure 3 is the scattered X-ray continuum, calculated using Equations 2 – 9 of Clark and Trombka (1997). The surface is simulated as a smooth high-K lunar basalt with a composition given by Taylor (1975) (Table 2). A lunar basalt composition may not be a close analogue for much of Mercury's surface, but basalt contains a rich mix of elements and is used here to give an indication of the fluorescence intensities that might be expected from the various elemental lines of interest. The lines shown are for solar quiet, B1, C1, and M1 flare states. The ability of MIXS to resolve individual lines is discussed in Section 10.

7 Magnetospheric Phenomena and X-ray emission

X-ray emission may also result directly from magnetospheric phenomena (for reviews of Mercury's magnetosphere see Ness, 1979; Russell et al., 1988; Slavin, 2004; Milillo et al., 2005). Mariner 10 showed that Mercury has a largely dipolar magnetic field tilted only slightly to the planetary spin axis. Interaction of this magnetic field with the solar wind creates a miniature magnetosphere, capable of standing off the solar wind to a distance of ~1.5 R_M (where 1 R_M is 2439 km). However, the nature of the internal dynamo is yet to be fully understood. Nevertheless, Mariner 10 observations left the impression that Mercury's magnetosphere is potentially one of the most dynamic in the solar system, showing evidence of familiar terrestrial magnetospheric processes. These include dayside magnetic reconnection phenomena (or Flux Transfer Events - FTEs) similar to those seen at the Earth, ULF wave activity (indicative of closed field lines), and

extremely rapid substorm activity on time-scales of a few tens of seconds. It is possible that these processes will produce X-rays at the surface of the planet (or even in the exosphere) due to precipitation and/or acceleration of electrons and/or ions in large scale current systems associated with solar wind-magnetosphere-exosphere-surface coupling (for example, see Grande, 1997; Burbine et al., 2005). Burbine et al. (2005) have suggested that electron-induced X-ray emission from Mg, Al and Si should be detectable by the MESSENGER X-ray Spectrometer (XRS) on the dark side of Mercury.

If this is the case, MIXS would sample the surface/exosphere effects of this dynamic coupling, which *in situ* plasma and field measurements alone will not be able to establish. Candidate processes which may produce surface X-ray emission are: cusp dynamics or FTEs, substorms/Pi2 pulsations (irregular and damped ultralow frequency range magnetic pulsations which occur in connection with magnetospheric substorms), and the effects of active solar wind conditions (i.e. Solar Energetic Proton events (SEPs) and Coronal Mass Ejections (CMEs)). To fully understand the magnetospheric phenomena, of which X-ray emission is one manifestation, it will be important to coordinate measurements by MIXS with *in situ* field and plasma measurements taken with instruments on both the MMO and MPO spacecraft.

8 The Mercury Imaging X-ray Spectrometer (MIXS)

The optical elements for both instrument channels, shown schematically in Figure 1, consist of microchannel plate (MCP) X-ray optics operating in two different modes and manufactured by Photonis SAS (Brive, France). MIXS-T has radially packed, square-pore MCPs in a Wolter Type I optical geometry (Willingale et al., 1998). MIXS-C has

451 square packed, square-pore MCP optics in a "slumped collimator" optical geometry.
452 Figure 4 shows a scanning electron microscope image of an MCP coated with a thin layer
453 of Ir to optimise its X-ray reflectivity (Jefimovs et al., 2007). The MCPs for both
454 telescope and collimator have a high reflectivity 60 nm thick Al film over their front
455 faces, to reduce thermal load. Microchannels are arranged in square multifibres, which
456 are then stacked in the appropriate geometry.
457

458 **8.1 The MIXS focal plane assembly**

459 Both MIXS-T and MIXS-C have identical focal plane assemblies, based on monolithic
460 19.2 mm × 19.2 mm Active Pixel Sensors (APS). The sensor features Macropixels
461 (Zhang et al., 2006), which combine the benefits of DEPFET (DEpleted P-channel Field
462 Effect Transistor) structure (Treis et al., 2006) (i.e. low power consumption, fast readout,
463 excellent energy resolution at low noise, intrinsic radiation hardness and arbitrary access
464 to pixels) with those of a Silicon Drift Detector (SDD) (arbitrary scalable pixel sizes and
465 an entrance window with low X-ray attenuation).
466

467 The FWHM energy resolution (ΔE) of the Gaussian detector response is given by

468 $$\Delta E = 2.36w\left(\frac{FE}{w} + R^2 + A^2\right)^{\frac{1}{2}}, \quad (2)$$

469 where w is the energy required to create an electron hole pair (3.62 eV in Si), F is the
470 Fano factor (a factor describing the non-Poissonian variance in the number of electrons
471 generated in a detector by an incident X-ray photon, ~ 0.1 in Si) (Fraser, 1989), E is X-
472 ray energy and R and A are the noise contributions from the readout electronics and

amplification (Fraser, 1989). Measurements of X-ray spectra obtained by DEPFET detectors by Zhang et al. (2006) have shown that energy resolutions approaching the theoretical Fano limits (~60 eV at 1 keV, 130 eV at 6 keV) are feasible with these devices.

The MIXS detectors will measure X-rays in the energy range 0.5 – 7.5 keV, with a spectral resolution of 100 eV at 1 keV at the start of operations, following the 6 year cruise to Mercury. The resolution will degrade over the mission lifetime due to radiation damage but should still be less than 200 eV after one year at Mercury (Treis et al., 2008).. This resolution allows the separation of X-ray line emission from elements of interest while the predicted sub-keV quantum efficiency permits the detection of lines not accessible to previous instruments - including the Fe-L emission line at 0.7 keV. This measurement is vital in elucidating the apparent low iron abundance indicated by ground-based visible and infrared spectroscopy (which is sensitive to Fe-O bonds rather than to Fe itself). Fe-L is of particular importance because the higher energy Fe-K lines (6.40 keV and 7.06 keV) are practically visible only during high solar states.

The MIXS focal plane assembly (FPA) consists of a 64 × 64 array of 300 μm macropixels, each with a triple drift ring structure. Whereas in a charge coupled device (CCD), charge is transferred across the whole device for readout by a single preamplifier, in the macropixel array every pixel has its own readout FET (Field Effect Transistor). The predicted quantum efficiency (QE) of the MIXS detector is shown as a function of

energy in Figure 5. The window is 30nm polyimide plus 50nm Al, with negligible X-ray attenuation above 0.5 keV.

8.2 MIXS-C optics

An X-ray collimator is conventionally an array of parallel channels whose aspect ratio (the ratio of channel length L and width d) alone defines the field of view (FOV). The collimator is positioned directly above an underlying detector and the two have identical areas. Such a geometry means that the effective area of a planar collimator falls off linearly with off-axis angle; the angular response is triangular in form (Fraser 1989). In contrast, MIXS-C uses a slumped or radial collimator geometry, shown schematically in Figure 6. This geometry allows (a) the reduction of the required detector size for a given collimator aperture and (b) the physical separation of the collimator and detector planes, with consequent advantages in terms of cost, radiation shielding mass, cooling power and sensitivity.

The MIXS-C collimator is an array of four slumped 40 × 40 mm square pack - square pore glass MCPs with 20μm wide channels. The MCPs are spherically slumped to a common radius of 550 mm and have a channel aspect ratio of 55:1. The open area fraction of the MCPs is 0.6, comparable with that of a standard mechanical collimator. The side length D of the square collimator is 80 mm and the detector is square, with a side length of 19.2mm, identical to the MIXS-T detector. The detector is placed 550 mm from the collimator along the optical axis, at the collimator's centre of curvature. In this geometry, the FOV for collimated X-rays is determined by the sum of the angle subtended by the slumped collimator and the acceptance angle of the channels, and is

518 equal to 10.4°. The design ensures that all X-rays transmitted through the collimator are
519 ultimately incident on the detector.
520
521 In addition to the collimated flux , X-rays can be reflected from the Ir-coated internal
522 faces of the microchannels. Figure 7 shows the effective areas (transmitted, transmitted
523 plus reflected rays) as a function of angle for MIXS-C at 1 keV, calculated using the
524 Monte-Carlo raytracing model of Price et al. (2002),. Unlike a conventional collimated
525 instrument, MIXS-C's effective area is constant across most of its FOV. The FOV can be
526 described by two components (i) a core FOV defining the central "flat top" angular
527 response (6.5°) and (ii) the total FOV incorporating the fall-off in effective area to zero
528 (10.4°).

529 **8.3 MIXS-T optics**

530 MIXS-T uses radially-packed, 20 μm square-pore MCP optics, in a conical
531 approximation to the Wolter type I focussing geometry, typically used in X-ray
532 astronomy (Ashenbach, 1985). The MCP embodiment of the Wolter optic geometry is
533 discussed in detail by Willingale et al. (1998); the path of an X-ray through an MCP
534 Wolter pair is illustrated in Figure 8. The focal length of MIXS-T is 1 m, determined by
535 the 4 m and 1.33 m slump radii of the front and rear MCP plates (Willingale et al. 1998).
536 X-rays entering a microchannel in the first plate are reflected at grazing incidence from
537 an internal channel wall, upon exiting the front MCP, the X-ray then enters a
538 microchannel in the rear MCP where a second reflection takes place. After two
539 reflections, the beam converges in the focal plane. Deviations from the optimal path of
540 an X-ray may occur due to multiple reflections within microchannels, misalignments

between microchannels and groups of microchannels (multifibres) or because of scattering due to small deviations from a perfectly smooth Ir-coated reflective channel walls. The achievable quality of the focus is ultimately limited by the practical approximation to the radial packing geometry and by the conical approximation to the true Wolter I geometry.

The 210 mm diameter MIXS-T optic, shown in Figure 1 and schematically in Figure 9, is assembled from a mosaic of MCPs, each of which is a sector of a circle, slumped to the figure of the surface of a sphere. Front and rear "sectors" together form "tandems" which are arranged in three rings with different thicknesses (2.2 mm inner, 1.3 mm middle, and 0.9 mm outer) to approximate the ideal 1/r thickness profile which maximises the throughput of the telescope by maximising the probability of a single reflection in each MCP.

The on-axis effective area of the MIXS-T optics has been calculated using a Monte Carlo ray-tracing model incorporating the geometric parameters given above. The mechanical support structure of the telescope, illustrated in Figure 1, is accounted for and perfect stacking of microchannel multifibres is assumed. The on-axis effective area for the MIXS-T optics (not including the detector efficiency) as a function of energy is shown in Figure 10 both for rays which are truly focused (labelled "focussed") and for all rays incident in the focal plane, including those which undergo scattering or multiple reflections inside the microchannels (labelled "focal plane"). Counting all rays in the focal plane, both focussed and non-focussed, provides a means of maximising the

564 counting rate for any given elemental line, gaining sensitivity at the expense of spatial
565 resolution. Raytracing indicates that the likely limiting resolution for the MIXS-T optics,
566 assuming perfect alignment of microchannels, multifibres and sectors is ~1 arc minute..
567 The formal science requirement for MIXS-T is to achieve an angular resolution better
568 than 9 arc minutes.
569
570 The effective area of MIXS-T decreases with off-axis angle, because the X-ray
571 reflectivity decreases with increased grazing angles to the channel walls, and the
572 reflection geometry along the channels becomes less favourable for single reflections in
573 both front and rear MCPs. This reduction in effective area with off-axis angle is the so-
574 called vignetting function and is shown for four X-ray energies in Figure 11.

575 ### 8.4 MIXS Grasp

576 The collecting power of both MIXS channels can be described in terms of the product of
577 effective area and field of view - which in astronomy is known as the Grasp, $G(E)$ (units
578 of cm^2 sr – derived below for a telescope in equation 6). Where X-rays in the energy
579 interval $E,E+dE$ are emitted from an extended source (i.e. the surface of Mercury) and
580 are incident on the instrument aperture with a flux $I(E)$ (in photons cm^{-2} s^{-1} steradian^{-1}
581 keV^{-1}) then the number of detected photons C detected in a time t is given by
582 $$C = I(E)G(E)tdE\,. \quad (3)$$
583 The calculated $G(E)$ for MIXS-C shown in Figure 12, is the result of multiplying the
584 field of view (0.033 steradians), by the geometrical area of the collimator (64 cm^2) while
585 taking into account the raytraced transmission of the collimator geometry and the
586 detector QE. Also included is the X-ray transmission of a 60 nm Al thermal filter on the

input face of the microchannel plates, and an additional 100nm of Al on 300nm of polyimide as an optical filter directly in front of the focal plane array. The calculated Grasp at 1 keV is 0.032 cm^2 sr.

Let us consider a "focusing" collimator and planar collimator of equal aperture; a planar collimator would have a grasp of ~0.096 cm^2 sr, a factor of ~3 larger than MIXS-C, However, this requires a factor of 16 greater focal plane area, which is limited for MIXS (cooling power, cost, development time). Therefore, a planar collimator would be unsuitable for MIXS and the advantages of using a focusing collimator are clear.

The grasp, *G,* for an imaging telescope (MIXS-T) can be calculated from the on-axis effective area $A(0,E)$ and the vignetting function. For an instrument with a circular FOV the element $d\Omega$ of solid angle subtended by an angular element $d\xi$ at an off-axis angle ξ is approximated at small off-axis angles by

$$d\Omega = 2\pi\xi d\xi \tag{2}$$

and the off-axis effective area $A(\xi,E)$ is

$$A(\xi, E) = A(0, E)V(\xi, E), \tag{3}$$

The grasp $G(E)$ is given by

$$G(E) = 2\pi\varepsilon_d(E)T(E)A(0,E)\int_0^{\xi_{\max}}\xi V(\xi, E)d\xi, \tag{4}$$

where $\varepsilon_d(E)$ is the detector QE and $T(E)$ is the combined transmission of the optical and thermal filters in front of the detectors.

An approximation to the vignetting function can be obtained by assuming that there is a linear fall off from the peak on-axis effective area to a minimum of zero at the edge of the field of view, which is defined by the 19.2 × 19.2 mm detector, which at a 1m focal length gives an FOV of 1.1° (0.55° half angle). Using this approximation for the vignetting function and assuming a perfect detector and 50cm^2 on axis effective area, G is estimated to be ~0.009 cm^2 sr. Figure 12 shows the MIXS-T grasp (*G(E)*), incorporating a more realistic vignetting function generated by Monte-Carlo raytracing software (Figure 11), the detector's QE and the calculated absorption of a 60 nm thick Al thermal filter on the input optic surface and a 100 nm Al optical filter deposited on 300nm of polyimide. The grasp is calculated for both focussed X-rays and for all rays incident in the focal plane, as shown in Figure 10,.

9 Instrument background levels and minimum detectable flux

The sensitivity of a photon-detecting instrument can be quantified by the minimum detectable flux I_{min}, which is the minimum signal flux from a source that can be distinguished from the background B. We assume that an isotropic flux I (in units of photons cm^{-2} s^{-1} sr^{1}) of fluorescent X-rays at a discrete energy (in keV) from an extended source is incident on the front of an instrument with a grasp G. This instrument has a focal plane detector with an area for photon detection A_{det} and energy resolution δE. The

633 detected fluorescent X-ray signal is accompanied by a background of solar X-rays which
634 are scattered from the surface under examination, denoted by I_{scat} (in units of photons cm^{-2} s^{-1} sr^{-1} keV^{-1}).
635
636
637 Although features in the scattered continuum may contain information on surface
638 properties and absorption features in the continuum may yield compositional information,
639 in terms of measuring fluorescence spectra the continuum constitutes a background and is
640 treated as such here. The detector also has a non-X-ray background component, caused
641 by charged particle events B_p (units of events cm^{-2} s^{-1} keV^{-1}). For a cooled, photon-
642 counting detector, intrinsic thermal noise is negligible and the scattered X-ray component
643 and the particle induced background will dominate. If a signal to noise ratio R is required
644 for the detection of an X-ray line then I_{min} may be defined as the flux that, in a given
645 integration time, produces a count R standard deviations of B above its mean. I_{min} for a
646 given value of R (typically taken to be 3 -5) is given by

647 $$I_{\min} = \frac{R\sqrt{\delta E(B_p A_{\det} + I_{scat} G)}}{G\sqrt{t}}. \quad (5)$$

648
649 The particle-induced X-ray background B_p results from a combination of both high
650 energy cosmic rays and lower energy (10-100 MeV) protons ejected from the Sun. To
651 reduce B_p MIXS's detectors are shielded by 15 mm of Al, which is the Continuous
652 Slowing Down Approximation (CSDA) range for 60 MeV protons in Al.
653
654 In the absence of direct measurements at Mercury, in order to calculate the expected
655 instrument background, we must use data for the integrated intensities of solar X-rays and

656 protons in various energy bands, measured in geostationary orbit at 1 AU by the
657 Energetic Particle Sensor (EPS) on the GOES spacecraft (Sellers et al., 1996). EPS data
658 show a poor correlation between the flux of protons with energies > 60 MeV and X-ray
659 flux for most solar conditions, and for lower energy protons the flux can be highly
660 variable. For high (M – X) X-ray flare states, however, the flux of > 60 MeV protons may
661 increase by several orders of magnitude, with the peak in proton flux occurring some time
662 after the X-ray flux. At 1 AU the time delay between the peaks in the X-ray and proton
663 fluxes during an X-flare is typically of the order 2 hours. At Mercury the delay will be
664 between approximately 35 and 55 minutes for perihelion and aphelion, respectively. The
665 MIXS background count rates due to solar protons will typically vary by less than one
666 order of magnitude for the majority of the instrument lifetime. Very large solar flares may
667 however be followed, within an hour, by an increase in background of several orders of
668 magnitude.
669
670 We have estimated the MIXS background at Mercury by scaling that experienced by the
671 XMM Newton X-ray observatory's EPIC X-ray camera's pn-CCDs (Strüder et al., 2001)
672 which are in a highly elliptical orbit around the Earth. These are analogous to the MIXS
673 detectors and are considered useful for comparison with MIXS. . Cosmic ray and solar
674 proton events in the EPIC pn detectors are rejected on the basis of energy, or the shapes
675 of tracks left by particles as they deposit energy in adjacent pixels. The post-rejection
676 background rate for the pn-CCDs is reported to be 0.039 cm^{-2} s^{-1} in the energy band 0-10
677 keV (Lumb, 2002) giving a count rate per keV of 0.0039 cm^{-2} s^{-1} keV^{-1}. XMM Newton's
678 CCDs have 30mm Al shielding for the detectors which can be penetrated by particles

679 with energies > 90 MeV. The fluxes for >90 MeV protons are typically a factor 2-3 less
680 than for > 60 MeV protons (Xapsos, 2000). The proton flux at Mercury for all energies
681 can be assumed to scale relative to that at 1 AU according to an inverse square law
682 dependence on the distance from the Sun (Mukai, 2003).
683
684 The energy deposited by minimum ionising particles (MIPS) in a silicon X-ray detector is
685 a function of the distance travelled in a single detector pixel and has been simulated by
686 Strüder (2000) who shows that for a 150μm × 150μm × 300μm Si pixel the Landau
687 energy distribution peaks at about 40 keV. This peak corresponds with a most probable
688 distance travelled in a single pixel of 150μm. Scaling this distribution to account for the
689 larger MIXS pixel size (300 × 300 × 450 μm) gives a peak at 80 keV and approximately
690 10% of energy deposited by MIPS will be in the energy band 0-10 keV. The MIXS
691 energy band is from 0.5-7.5 keV. The distribution varies little over the range 0-10 keV
692 and it is therefore assumed to be constant within this energy range. Consequently, a
693 background rate in the 0.5-7.5 keV energy band of 0.04 cm^{-2} s^{-1} keV^{-1} is calculated.
694
695 If a three order of magnitude increase in flux is assumed after high flare states then the
696 background rate may reach values of 40 cm^{-2} s^{-1} keV^{-1}. The background value given for
697 the XMM-Newton detectors, however, includes galactic cosmic rays and solar protons
698 and it is inappropriate to scale the former event rate with distance from the Sun. Solar
699 protons are believed to contribute only ~10% of the XMM background at 1 AU on
700 average (Strüder, 2000). If only 10% of the 1 AU background value attributable to SEPs
701 is scaled to 0.31 AU then the typical MIXS background under normal conditions is

estimated to be ~0.008 cm^{-2} s^{-1} keV^{-1}. We have therefore adopted 0.04 cm^{-2} s^{-1} keV^{-1} as a worst-case background rate.

10 The detection of elements by MIXS

Using Equation 7 we have calculated the time required for 3σ detection of the various elemental lines of interest in different solar flare states, for which the incident solar spectra are shown in Figure 2. It is assumed that a minimum of ten photons is required for a significant detection. The calculated integration times for MIXS-T and –C are shown in Table 3 and Table 4 respectively. A worst case value of 0.04 cm^{-2} s^{-1} keV^{-1} is assumed for the particle background B_p. The L shell emission lines of Ti and Cr are coincident with the far more intense O-K line and therefore cannot be separated and are not included here. Where the required integration times are longer than 1 year, an element is considered to be undetectable and is left blank in the tables. The spatial scales on which elements may be measured are defined by the required integration times, the instrument FOVs and by the orbital velocity of the BepiColombo MPO. The imaging capability of MIXS-T allows data to be manipulated for optimum imaging or spectroscopy. For MIXS-T it is assumed initially that all photons in the focal plane are added together and the imaging capability within the field of view is not applied, this optimises the measurement statistics for spectroscopy. For times where the flux from Mercury is high, the imaging capability of MIXS-T can be applied, by subdividing the focal plane into its imaging pixels, the application of imaging to various elements is discussed below.

The number of counts from single surface elements can be maximised by combining measurements made of the same surface area during multiple passes overhead (using the

725 solar spectrum, as measured by SIXS to allow normalisation between subsequent orbits).
726 The coverage time achieved as a function of position on the surface has been calculated
727 using the Satellite Tool Kit (STK) (Analytical Graphics Inc.) for illuminated segments of
728 the planet during one year of operations beginning in September 2019. The resultant
729 coverage map for MIXS-T is shown in Figure 13 and for MIXS-C in Figure 14. The
730 nodes used in the calculation are positioned on the surface at 4° latitude and longitude
731 intervals. The structure visible in the images is a combination of the node spacing and the
732 effect of including only dayside observations in the measurements. Typical accumulated
733 coverage times for near-equatorial regions of approximately hundreds of seconds increase
734 to more than three hundred seconds at high latitudes. For MIXS-C we calculate
735 accumulated coverage times of ~9000 seconds in near-equatorial regions, increasing to
736 almost 30000 seconds at high latitudes. Assuming a "worst case" scenario in which all
737 measurements of a surface element are made during solar quiet, the number of counts
738 expected for MIXS-T is shown in Table 5 and for MIXS-C is shown in Table 6, assuming
739 nadir viewing and normal incidence for solar X-rays. A more typical scenario would see
740 ~20% of the year in B-flare state during solar minimum (Huovelin et al., this volume).
741 The percentage errors shown in the tables correspond to the Poissonian errors in the
742 number of counts.
743
744 The dwell times for a surface element (the time between a point on the surface entering
745 and then leaving the FOV) during single passes by MIXS-C at apoherm and periherm are,
746 respectively, 209 and 27.9 seconds. For MIXS-T, the dwell times at apoherm and
747 periherm are 22.1 and 3.0 seconds. Measurements made in a single surface element

748 during solar flare events will contain many more counts than during solar quiet and
749 provide access to X-ray lines with higher energies than can be measured during low solar
750 flare states. Simulated spectra for single passes at apoherm (1500 km altitude) are shown
751 for MIXS-T in Figure 15 and for MIXS-C in Figure 16. The spectra assume nadir
752 pointing and normal incidence for solar X-rays at a Sun-Mercury distance of 0.39 AU.
753 The detectors have 40 eV energy bins and, for illustrative purposes, the surface is
754 assumed to have the lunar high-K basalt composition of Table 2. We assume a FWHM
755 energy resolution of 100eV at 1 keV, varying as a function of energy according to
756 Equation 3. In the period after an X-flare, the solar proton flux may (in extreme cases)
757 increase by five orders of magnitude, implying a particle-induced background in the
758 detector of 400 cm^{-2} s^{-1} keV^{-1}. If X-flare intensities are maintained in the period post flare
759 then the sensitivity of the instrument to weaker K_β lines is reduced but does not alter the
760 sensitivity to the more intense K_α lines shown here, other than for P-K_α which can no
761 longer be detected. This is primarily because the background due to the scattered X-ray
762 continuum is typically much greater than the proton-induced background. The enhanced
763 proton flux following a flare can take several days to decay, while the X-ray flux returns
764 to typical values within hours. During these periods, the proton background may remain
765 sufficiently high relative to the X-ray signal that measurements may be compromised.
766
767 The imaging capability of MIXS-T allows measurements from surface areas smaller than
768 the surface footprint of the 1.1° FOV. For M1 and X1 flares (assuming that the incident
769 solar intensity for an X1 flare = 10 M1), Table 8 gives an estimated spatial resolution
770 achievable from apoherm for key elements which still give a statistically significant

771 measurement as described in Section 5 and summarised in Table 7. A maximum
772 resolution of 2 arc minutes is reported in the table as this is the goal of the MIXS-T
773 optics, although the formal requirement is for an angular resolution of less than 9 arc
774 minutes. The grasp values for focussed rays only are used in these calculations.
775
776 Global abundance averages for elements may be measured by integrating spectra
777 accumulated during the entire mission. Table 9 shows the total number of counts in major
778 elemental lines expected for MIXS-C in one year, assuming a worst case scenario in
779 which all measurements are made during solar quiet and assuming measurements are
780 made at 0.39 AU. A mean angle for incident solar X-rays of 45° is assumed and only
781 dayside measurements are considered.
782
783 However, unless Mercury has only one widespread type of crust, combining
784 measurements to give global averages may obscure important variations and result in
785 geologically uninformative results. Because of the divergent formation mechanisms for
786 primary and secondary crust (Section 4), it will be more useful to make separate
787 calculations of average element abundances in primary and secondary crust. To separate
788 the two sets of measurements, we will use data from other BepiColombo experiments
789 (notably SIMBIO-SYS and MERTIS) to help to map the extent of each crustal type.

790 **10.1 Validation of the fluorescence model**

791 To validate our X-ray spectral calculations, we compare X-ray spectra of the Moon, made
792 by the Chandra X-ray observatory ACIS instrument and presented by Wargelin et al.
793 (2004), with synthetic spectra generated using the fluorescence model presented above.

794 The Chandra observations were made in July 2001 using the I2 and I3 front illuminated
795 chips of the Advanced CCD for Imaging Spectroscopy (ACIS) focal plane instrument
796 (Garmire et al, 2003).
797
798 The GOES X-ray data sets for the period of the Chandra observations of the Moon
799 typically show a mid B-flare state. In the following simulations, a B2 flare state is
800 modelled as a B1 flare, as in Figure 2, multiplied by two, independent of energy. The
801 composition of the large areas of the lunar surface observed by Chandra is unknown; the
802 modelled spectra represent the two possible lunar soil compositions given by Clark and
803 Trombka (1997); Apollo 16 Highlands and Apollo 12 mare basalt. The calculations
804 assume that the illuminated lunar surface is perfectly smooth. The illumination angle θ
805 and the observation angle ϕ are taken to be 45°, approximating the geometry illustrated
806 by Wargelin et al. (2004). The I2 and I3 effective area as a function of energy for the
807 ACIS-I instrument was determined from the Chandra Science Data Center
808 (http://asc.harvard.edu/proposer/POG/). The FWHM energy resolution of the measured
809 spectrum presented by Wargelin et al., (2004) is ~111 eV at the O-K line (0.525 keV) and
810 is scaled to other energies here according to Equation 3. The aperture of a single ACIS-I
811 CCD is 5.9×10^{-6} steradians and the combined I2 and I3 integration time is 8063 s
812 (Wargelin et al, 2004). The simulated spectra are shown in Figure 17 along with the
813 measured peak count rates for O-K, Fe-L and Si-K.. There is good agreement between
814 measurement and model; in particular, this comparison demonstrates the feasibility of
815 detecting iron in planetary regoliths at all solar states via the L-shell emission.
816

817 The correct interpretation of X-ray measurements from the surface of Mercury will
818 require a detailed understanding of the processes that generate X-rays and the effects of
819 observing a real planetary surface as opposed to an idealised surface as modelled herein.
820 Theoretical and experimental investigations are proceeding to investigate the effects of
821 surface and regolith properties on emission spectra. Investigations are also ongoing into
822 the likely properties of the Mercurian magnetosphere and the X-ray emission that may
823 result from its interaction with the surface and exosphere as well as the solar wind. The
824 results of these investigations will be reported in future papers.

825 **11 MIXS at Mercury**

826 By accumulating data globally and/or for regions representing primary and secondary
827 crust, we expect to be able to measure at least Na, Mg, Al, Si, P, K, Ca, Ti, Fe and Ni
828 (although separation of the Ni-L line from the much more intense O-K line may prove
829 challenging), all to a high statistical precision. These data can be subdivided into data
830 from the various, large scale, Mercurian terrains. If Mercury has exposed primary crust as
831 well as secondary crust, subsets of data, representing areas dominated by primary crust
832 and areas dominated by secondary crust, will be more informative than global averages.

833 Under typical solar conditions MIXS-T will determine Na, Mg, Al, Si and Fe abundances
834 on scales of some tens of km, and MIXS-C will achieve scales of hundreds of km with
835 greater numbers of counts to provide increased statistical certainty for the spectral lines.
836 During solar flares, MIXS-C will have the capability to measure P, K, Ca, Ti, Cr, while
837 Na, Mg, Al, Si and Fe will be measured with increased statistical certainty. Spatial scales
838 of hundreds of km are sufficient to subdivide the surface of Mercury into the individual
839 terrains identified on Mariner-10 images; for example heavily cratered terrain and

840 intercrater plains (possibly both primary crust), smooth plains (probably secondary crust)
841 and 'hilly and lineated terrain' and 'hummocky plains' (probably impact-modified
842 versions of other terrain units) (e.g. Trask and Guest, 1975; Strom, 1997; Strom and
843 Sprague, 2003). It may be possible to distinguish differences in composition between
844 individual lava flows in compound flow fields to indicate the fractionation history of
845 magma chambers or the time-related depth of magma sources.
846
847 Highest spatial resolution measurements of just a few km will be achieved by MIXS-T
848 during solar flares for the major elements Na, Mg, Al, Si, P, K, Ca, Ti, Fe. These
849 measurements will provide access to a wide range of landforms including possible
850 volcanic constructs, craters of various diameters and depths as well as their central peaks.
851 The latter are uplifted material from the middle or lower crust and so may expose strata
852 formed during various eras in Mercury's history (including primary crust, which will be
853 important if it is not widespread at the surface) and/or bodies of magma intruded into the
854 crust. The youngest craters and their ejecta may also provide information on the rate and
855 nature of space weathering.
856
857 MIXS observations of X-ray emission from Mercury will allow the determination of
858 elemental abundances with unprecedented spatial resolution for a range of elements of
859 key importance for understanding the geology, evolution and formation of the planet. X-
860 ray emission will also provide a mechanism for investigating the unique surface-
861 magnetosphere interactions at Mercury.
862

Since preparation of this paper, the Messenger flyby data from the Gamma-ray spectrometer has been able to place a 0.5 wt % upper limit on the potassium content of the equatorial regions of Mercury. This is shown to rule out formation models which include k-rich feldspar. Future observations of this kind will be used to inform and improve the performance predictions for MIXS at Mercury. To date, a number of assumptions about the nature of the planet's surface have been made which were constrained only by our knowledge of the properties of the regolith and the superficial resemblance of Mercury to the Moon.

12 Acknowledgements

We thank the European Space Agency's BepiColombo team and Peter Nieminen of ESA for providing a detailed description of the polynomial approximations to Solar X-ray spectra. MIXS is supported by the Science and Technology Facilities Council (STFC) in the UK, TEKES in Finland, The Max Planck Society in Germany and INTA in Spain.

13 References

Adler, I and Trombka, J.I., 1970. Geochemical exploration of the Moon and planets, Springer-Verlag, New York.

Adler, I., Gerard, J., Trombka, J., Lowman, P., Blodgett, H., Yin, L., Eller, E., Lamothe, R., 1972. The Apollo 15 X-ray fluorescence experiment, Proc. Lunar Sci. Conf. 3rd, 3, 2157-2158.

884 Adler, I., Trombka, J. I.., Schmadebeck, R., Lowman, P., Blodget, H., et al., 1973.
885 Proceedings of the Lunar Science Conference, 4, 2783.
886
887 Ashenbach, 1985. X-ray telescopes, Rep. Prog. Phys., 48, 579-629.
888
889 Basaltic Volcanism Study Project, Basaltic volcanism on the terrestrial planets, 1981.
890 sponsored by the Lunar and Planetary Institute, Pergamon Press, New York, 1286 pp.
891
892 Benz, W, Slattery, W.L., Cameron, A.G.W., 1988, Collisional stripping of Mercury's
893 mantle, Icarus, 74, 516-528.
894
895 Benz, W., Anic, A., Horner, J., Whitby, J.A., 2007, The origin of Mercury, Space Science
896 Reviews, DOI 10.1007/s11214-007-9284-1.
897
898 Bland, P. A. and Benedix, G. K., 2006. Volatile depletion: Constraints from differentiated
899 meteorites. Meteoritics & Planetary Science 41, A22-A22.
900
901 Blewett, D. T., Hawke, B. R., Lucey, P. G., 2002, Lunar pure anorthosite as a spectral
902 analog for Mercury, Meteoritics and Planetary Science, 37, 1245-1254.
903
904 Brodrick, D., S. Tingay, and M. Wieringa, 2005. X-ray magnitude of the 4 November
905 2003 solar flare inferred from the ionospheric attenuation of the galactic radio
906 background, J. Geophys. Res., 110, A09S36, doi:10.1029/2004JA010960.

907

908 Burbine, T. H., Trombka, J. L., Bergstrom Jr., P.M. and Christon, S.P., 2005, Calculating
909 the X-ray Fluorescence from the Planet Mercury due to High Energy Electrons, LPSC
910 XXXVI, no. 1415.

911

912 Cameron, A.G.W., 1985, The partial volatilization of Mercury, Icarus, 71, 337-349.

913

914 Cameron, A.G.W., Fegley, B., Benz, W. and Slattery, W.L., 1988. The Strange Density
915 of Mercury: Theoretical Considerations, In Mercury, Eds. M.S. Matthews, C. Chapman
916 and F. Vilas, University of Arizona Press, Tucson, 692 – 708.

917

918 Clark, P.E., S.R. Floyd and J.E. Trombka, 1997. The Effectiveness of the Proportional
919 Counter as a Solar X-Ray Monitor for the NEAR Mission, Conference on the High
920 Energy Radiation Background in Space, Workshop record, 90.

921

922 Clark, P.E. and J.I. Trombka, 1997. Remote X-ray fluorescence experiments for future
923 missions to Mercury. Planet. Space. Sci, 45, 57-65.

924

925 Fichtel, C.E. and J.I. Trombka, 1997. Gamma Ray Astrophysics, New insight to the
926 Universe, 2nd Edition, NASA Ref. Publ., 1386.

927

928 Fraser, G.W., 1989. X-ray detectors in Astronomy, Cambridge University Press.

929

930 Fraser, G.W., A.N. Brunton, J.E. Lees, J .F. Pearson and W.B. Feller, 1993. X-ray
931 focusing using square-pore microchannel plates: First observation of cruxiform image
932 structure Nuc. Ins. and Meth. A324, 404-407.
933
934 Fegley, B. and Cameron, A.G.W., 1987. A vaporization model for iron/silicate
935 fractionation in the Mercury protoplanet, Earth and Planetary Science Letters, 82, 207-
936 222.
937
938 Garmire, G.P., Bautz, M.W., Ford, P.G., Nousek, J.A., Ricker, G.R., Jr., 2003, Advanced
939 CCD imaging spectrometer (ACIS) instrument on the Chandra X-ray Observatory,
940 Tananbaum. *Proc. SPIE*, 4851, 28-44.
941
942 Goettel, K.A., 1988. Present bounds on the bulk composition of Mercury - Implications
943 for planetary formation processes, In Mercury, Eds. M.S. Matthews, C. Chapman and F.
944 Vilas, Tucson, AZ, University of Arizona Press, 613-621.
945
946 Grande, M., 1997. Investigation of magnetospheric interactions with the Hermean
947 surface, Adv. Space. Res., 19, 1609-1614.
948
949 Grande, M., Browning, R., Waltham, N., Parker, D., Dunkin, S. K. et al., 2003. The D-
950 CIXS X-ray mapping spectrometer on SMART-1, Planetary and Space Science, 51, 427-
951 433.
952

953 Grande, M., Maddison, B.J., Sreekumar, P., Huovelin, J., Kellet, B.J., Howe, C.J.,
954 Crawford, I., Holland, A., and the CIXS team, 2008. The C1XS X-ray spectrometer on
955 Chandayaan 1. LPSC XXXIX, Abstract #1620.
956
957 Huovelin, J., Grande, M., Vainio, R., Malkki, A., Alha, L., Fraser, G.W., Kato, M.,
958 Koskinen, H., Muinonen, K., Naranen, J., Schmidt , W., Syrjasuo, M., Anttila, M.,
959 Vihavainen, T., Andersson, H., Kiuru, E., Roos, M., Valtonen, E., Peltonen, J., Talvioja,
960 M., Portin, P., Prydderch, M., 2008. Solar Intensity X-ray and particle Spectrometer
961 (SIXS), Planetary and Space Science, Present Volume.
962
963 Huovelin, J., Alha, L., Andersson, H., Andersson, T., Browning, R., Drummond, D.,
964 Foing, B., Grande, M., Hämäläinen, K., Laukkanen, J., Lämsä, V., Muinonen, K.,
965 Murray, M., Nenonen, S., Salminen, A., Sipilä, H., Taylor, I., Vilhu, O., Waltham, N.,
966 Lopez-Jorkama, M., 2002. The SMART-1 X-ray solar monitor (XSM): calibrations for
967 D-CIXS and independent coronal science, Planetary and Space Science, 50, 1345-1353.
968
969 Jefimovs, K., Vila-Comamala, J., Pilvi, T., Raabe, J. Ritala, M and David. C., 2007.
970 Zone-Doubling Technique to Produce Ultrahigh-Resolution X-Ray Optics, Physical
971 Review Letters, 99, 264801.
972
973 Jeanloz, R., Mitchell, D. L., Sprague, A. L., de Pater, I., 1995. Evidence for a basalt-free
974 surface on Mercury and implications for internal heat, Science, 268, 1455-145.
975

976 Leary, J. C., Conde, R. F., Dakermanji, G., Engelbrecht, C. S., Ercol, C. J., Fielhauer, K.
977 B., Grant, D. G., Hartka, T. J., Hill, T. A., Jaskulek, S. E., Mirantes, M. A., Mosher, L.
978 E., Paul, M. V., Persons, D. F., Rodberg, E. H., Srinivasan, D. K., Vaughan, R. M.,
979 Wiley, S. R., 2007, The MESSENGER spacecraft, Space Science Reviews, 131, 187-217.
980
981 Lowe, B.G., Holland, A.D., Hutchinson, I.B., Burt, D.J. and Pool, P.J., 2001. The swept
982 charge device, a novel CCD based EDZ detector: first results, Nucl. Inst. Meth. A, 458:
983 568-579.
984
985 Lumb, D., 2002. EPIC in orbit background, Proc. New Visions of the X-ray Universe in
986 the XMM-Newton and Chandra Era, ESA SP-488.
987
988 Margot, J.L., Peale, S.J., Jurgens, R.F., Slade, M.A., and Holin, I.V., 2007. Large
989 longitude libration of Mercury reveals a molten core, Science, 316, 710-714.
990
991 Milillo, A., Wurz, P., Orsini, S., Delcourt, D., Kallio, E., Killen, R.M., Lammer, H.,
992 Massetti, S., Mura, A., Barabash, S., Cremonese, G., Daglis, I.A., De Angelis, E., Di
993 Lellis, A.M., Livi, S., Mangano, V. and Torkar, K, 2005. Surface-Exosphere-
994 Magnetosphere System Of Mercury, Space Sci. Rev., 117, 397–443.
995
996 Morgan, J.W. and Anders, E., 1980. Chemical composition of earth, Venus, and Mercury,
997 Proc. Natl. Acad. Sci. USA, 77, 6973-6977.
998

999 Mukai, T., K. Ogasawara and Y. Saito, 2003. An empirical model of the plasma
1000 environment around Mercury, Advances in Space research, 33, 2166-2171.
1001
1002 Ness, N.F., 1979. The Magnetosphere of Mercury, in Solar System Plasma Physics, vol.
1003 II, Eds. C.F. Kennel, L.J. Lanzerotti and E.N. Parker, North-Holland, New York, 185–
1004 206.
1005
1006 Näränen, J., Parviainen, H., Muinonen, K., Nygard, K., Peura, M. and Carpenter, J.D.,
1007 2008. Laboratory studies into the effect of regolith on planetary X-ray fluorescence
1008 spectroscopy, Icarus, under review.
1009
1010 Näränen, J., Parvianen, H. and Muinonen, K., 2007. X-ray fluoresence modelling for
1011 solar system regoliths: effect of viewing geometry, particle size, and surface roughness,
1012 Proceedngs of the 236th IAU Symposium: Near Earth objects, Our Celestial Neighbours:
1013 Opportunities and Risk, Cambridge University Press. doi:10.1017/S1743921307003298.
1014
1015 Okada, T., Particle Size Effect in X-Ray Fluorescence at a Large Phase Angle:
1016 Importance on Elemental Analysis of Asteroid Eros (433). Lunar Planetary Sci., 35,
1017 1927, 2004.
1018
1019 Okada, T., Shirai, K., Yamamoto, Y., Arai, T., Ogawa, K. et al., 2006. X-ray
1020 Fluorescence Spectrometry of Asteroid Itokawa by Hayabusa, Science, 312,. 1338-1341.
1021

1022 Price, G.J., A.N. Brunton,, M.W. Beijersbergen, G.W. Fraser, M. Bavdaz, J.-P. Boutot, R.
1023 Fairbend, S.-O. Flyckt, A. Peacock, E. Tomaselli, 2002. X-ray focusing with Wolter
1024 microchannel plate optics, Nuc. Ins. and Meth., A 490, 276–289.
1025
1026 Robinson, M. S., Taylor, G. J., 2001. Ferrous oxide in Mercury's crust and mantle,
1027 Meteoritics and Planetary Science 36, 841-847.
1028
1029 Russell, C.T., Baker, D.N. and Slavin, J.A., 1988. The Magnetosphere of Mercury, in
1030 Mercury, Eds. F. Vilas, C.R. Chapman and M.S. Matthews, University of Arizona Press,
1031 Tucscon, 514–561.
1032
1033 Schlemm C.E, Starr, R. D., Ho, G.C., Bechtold, K.E., Hamilton, S.A., Boldt, J.D.,
1034 Boynton, W.V., Bradley, W., Fraeman, M.E., Gold, R.E., Goldsten, J.O., Hayes J.R.,
1035 Jaskulek, S.E., Rossano, E., Rumpf, R.A., Schaeferm, E.D., Strohbehn, K., Shelton, R.G.,
1036 Thompson, R.E., Trombka J.I., Williams, B.D., 2007. The X-Ray Spectrometer on the
1037 MESSENGER Spacecraft, Space Sci Rev, 131, 393-415.
1038
1039 Sellers, F.B. and Hanser, F.A., 1996. Design and calibration of the GOES-8 particle
1040 sensors: the EPS and HEPAD, Proc. SPIE 2812, 353-364.
1041
1042 Shirai, K., Okada, T., Yamamoto, Y., Arai, T., Ogawa, K., Shiraishi, H.,
1043 Iwasaki, M., Arakawa, M., Grande, M, Kato, M., 2008, Instrumentation and performance
1044 evaluation of the XRS on SELENE orbiter. Earth Planets Space, 60, 277-281, 2008

Slavin, J.A., 2004. Mercury's Magnetosphere, Adv. Space Res., 33, 1859–1874.

Solomon, S.C., 2003. Mercury: the enigmatic innermost planet, Earth and Planetary Science Letters, 216, 441-455.

Sprague, A. L., Hunten, D.M. and Lodders, K., 1995. Sulfur at Mercury, elemental at the poles and sulfides in the regolith. Icarus, 118, 211–215.

Sprague, A. L., Hunten, D.M. and Lodders, K., 1996. Erratum. Icarus, 123, 247.

Strom, R.G., 1997. Mercury: an overview, Advances in Space Research, 19, 1471-1485.

Strom, G. and Sprague, A.L., 2003. Exploring Mercury: The Iron Planet, Springer Praxis, New York.

Strüder, L., High resolution X-ray imaging X-ray Spectrometers, 2000. Nuc. Inst. Meth. A, 454, 73-113.

Strüder, L., Briel, U., Dennerl, K. and 55 other authors, 2001, The European Photon Imaging Camera on XMM-Newton: The pn-CCD camera, Astronomy and Astrophysics, 365, L18-L26.

1068 Taylor, S. R., 1975. Lunar Science: A post-Apollo view, New York, Pergamon Press, Inc.

1069

1070 Taylor, S. R., 1989, Growth of planetary crusts, Tectonophysics, 161, 147-156.

1071

1072 Taylor, G. J. and Scott, E. R. D., 2004. Mercury, in Treatise in Geochemistry, Vol. 1.

1073 Meteorites, Comets, and Planets, Davis, A. M. (ed), Elsevier, 477-486.

1074

1075 Trask, N. J., Guest, J. E., 1975. Preliminary geologic terrain map of Mercury, Journal of

1076 Geophyscial Research, 80, 2461-2477.

1077

1078 Treis, J., Andricek, L., Herrmann, S., Heinzinger, K., Lauf, T., Lechner, P., Lutz, G.,

1079 Mas-Hesse, J.M., Porro, M., Richter, R.H., Schaller, G., Schnecke, M., Schopper, F.,

1080 Segneri, G., Soltau, H., Stevenson, T., Strüder, L., Whitford, C.W., Wölfel, S., 2008.

1081 DEPFET Based Focal Plane Instrumentation for X-ray Imaging Spectroscopy in Space;

1082 2007 IEEE NSS conference record, IEEE Catalog Number 07CH37869C, N47-3.

1083

1084 Treis, J., Fischer, P., Hälker, O., Harter, M., Herrmann, S., Kohrs, R., Krüger, H.,

1085 Lechner, P., Lutz, G., Peric, I., Porro, M., Richter, R. H., Strüder, L., Trimpl, M.,

1086 Wermes, N., 2006, Study of noise and spectroscopic performance of DEPMOSFET

1087 matrix prototypes for XEUS, Nucl. Inst. Meth. A, 568, 1, 191-200.

1088

1089 Trombka, J.I., Squyres, S.W., Brückner, J., Boynton, W.V. Reedy, R.C. et al. 2000. The
1090 Elemental Composition of Asteroid 433 Eros: Results of the NEAR-Shoemaker X-ray
1091 Spectrometer, Science, 289. 2101 – 2105.
1092
1093 Truscott, P., Dyer, C. and Peerless, C., 2000. Basalt X-ray fluorescence study, DERA
1094 report, DERA/CIS/CIS2/7/36/4/1/3.
1095
1096 Tucker W.H. and M. Koren, 1971. Radiation from a high-temperature low-density
1097 plasma: the X-Ray spectrum of the solar corona, The Astrophysical Journal, 168, 283.
1098
1099 Wargelin, B.J., Markevitch, M., Juda, M., Kharchenko, V., Edgar, R., and Dalgarno, A.,
1100 2004, Chandra observations of the "dark" Moon and geocoronal solar wind transfer, The
1101 Astrophysical Journal, 607, 596–610.
1102
1103 Weidenschilling, S.J., 1978, Iron/silicate fractionation and the origin of Mercury, Icarus,
1104 35, 99-111.
1105
1106 Willingale, R., Fraser, G.W., Brunton, A.N. and Martin, A.P., 1998. Hard X-ray imaging
1107 with microchannel plate optics, Experimental Astronomy. 8, 281-296.
1108
1109 Xapsos, M.A., Summers, G.P., Barth, J.L., Stassinopoulos, E.G. and Burke, E.A., 2000.
1110 Probability Model for Cumulative Solar Proton Event Fluences, IEEE Trans. Nucl. Sci.,
1111 47, 486-490.

Zhang, C., Lechner, P., Lutz, G., Porro, M., Richter, R., Treis, J., Strüder, L. Nan Zhang, S., 2006. Development of DEPFET Macropixel detectors, Nucl. Inst. Meth. A, 568, 1, 207-216.

Zombeck, M.V., 2007. Handbook of Space Astronomy and Astrophysics, Third Edition, Cambridge University Press.

Figure 1. A Schematic illustration of MIXS showing the adjacent MIXS-T and MIXS-C channels.

Figure 2. Polynomial approximations to the solar X-ray spectrum in M1, C1 and B1 flare states derived from various sources as described in the text together with measured solar X-ray spectra from the X-ray Solar Monitor (XSM) instrument on SMART 1. Also shown is the predicted magnitude of the diffuse X-ray background (DXB) measured by XSM between 3 keV and 7 keV.

Figure 3. Simulated fluorescence emission spectrum from a lunar basalt surface at 0.39 AU, under various solar flare conditions calculated using Equation 1. Lines are shown with a 2 eV width.

Figure 4. Scanning electron microscope image showing the Ir coated, square microchannel structure of an MCP X-ray optic.

Figure 5. Calculated quantum efficiency of the MIXS FPA detectors.

Figure 6. Geometry of the MIXS-C slumped collimator. The side length of the collimator is 80mm and the 550 mm separation of the MCP collimator and the detector is equal to the collimator's spherical slump radius. The acceptance half angle for a single channel is defined by its aspect ratio (L:d).

Figure 7. Raytraced effective area as a function of off axis angle for the Ir coated MIXS-C optics at 1 keV.

Figure 8. Illustration of the path of an X-ray through sections of the front and rear slumped MCP optic microchannels, which together are a conical approximation to a true Wolter type I optic. The three channel lengths shown correspond to the inner, middle and outer rings of the MIXS-T optic.

The channel side length in each case is 20µm and the thickness of the septal wall between microchannels is 6 µm.

Figure 9. Schematic diagram of the MIXS-T MCP Wolter optics in cross section (not to scale). The front MCPs are slumped to a radius of 4m. The rear MCPs are slumped to a radius of 1.33 m. The mosaics of MCPs are arranged in three rings of differing thicknesses which approximate an ideal 1/r profile in channel thickness (see text). Rays are reflected from the internal surfaces of both front and rear microchannels and are focussed at a distance of 1m from the optic. The MIXS-T optic as viewed from the front and showing the arrangement of the sectors and rings is shown in Figure 1. The middle section in the pattern does not contain an MCP optic – this area is masked by the telescope structure.

Figure 10. On-axis effective area for the MIXS-T MCP optics. Focused rays are those that arrive at the focus of the telescope. The focus of the telescope is defined by the FWHM of the peak generated on a detector by parallel rays entering the aperture, the effective area is calculated for all rays that are truly focused by the optics (one reflection in each MCP). Focal plane in the figure refers to all rays arriving in the focal plane, including non-focussed rays that have been scattered or undergone multiple reflections in the optics.

Figure 11. The reduction in effective area with off axis incident angle, relative to the on-axis value (vignetting) for MIXS-T at four different X-ray energies.

Figure 12. Grasp G as a function of energy for MIXS-T and MIXS-C. The structure indicated is the result of X-ray absorption by the Ir coating.

Figure 13. Hammer-Aitoff projection of Mercury showing the predicted day side coverage time as a function of latitude and longitude on Mercury for MIXS-T during one year of operations beginning in September 2019. Craters shown are major craters observed by Mariner 10.

Figure 14. Hammer-Aitoff projection of Mercury showing the predicted day side coverage time as a function of latitude and longitude on Mercury for MIXS-C during one year of operations beginning in September 2019. Craters shown are major craters observed by Mariner 10.

Figure 15. Simulated X-ray spectra for MIXS-T during a single 22.1 s pass at apoherm in various solar flare states and assuming normal solar illumination and a nadir viewing angle at 0.39 AU. The spectra have 100 eV FWHM energy resolution at 1keV and the bin width is 40 eV.

Figure 16. Simulated X-ray spectra for MIXS-C during a single 209 s pass at apoherm in various solar flare states and assuming normal solar illumination and a nadir viewing angle at 0.39 AU. The spectra have 100 eV FWHM energy resolution at 1keV and the bin width is 40 eV.

Figure 17. Simulated Chandra ACIS X-ray spectra of the Moon for highland and Mare lunar soil compositions. Also shown are peak values for the Chandra ACIS lunar X-ray spectrum presented by Wargelin et al. (2004). The energy bin width shown here is 30 eV.

Table 1 Percentage by mass of some major elements in Mercury's bulk silicate fraction for nine models of Mercury's formation, [1]Morgan and Anders, 1980; [2]Chapter 4, Basaltic Volcanism on the Terrestrial Planets, 1980; [3] models 3 of 4 of Fegley and Cameron, 1987; [4]Goettel, 1988).

Table 2. Compositions of rocks (% by mass for the main elements) in the lunar crust, to give an indication of the possible variability of composition that might be encountered during study of Mercury's crust. Also shown are the line energies for X-rays in the MIXS 0.5-7.5 keV energy band. The compositional data is derived from % mass oxides data from Taylor (1975). The mass fraction not shown is O.

Table 3. Integration times in seconds required for MIXS-T to detect various elements in different solar flare states assuming a high K lunar basalt surface composition.

Table 4. Integration times in seconds required for MIXS-C to detect various elements in different solar flare states assuming a high K lunar basalt surface composition.

Table 5. Counts detected by MIXS-T in 100s during solar quiet.

Table 6. Counts detected by MIXS-C in 9000 s during solar quiet.

Table 7. The minimum precision required to allow for significant interpretation of measurements for possible minimum % mass values of various elements at Mercury. The table condenses the requirements from Section 5. A failure to meet one of these requirements does not necessarily detract significantly from the science as other elemental measurements may be sufficient. The % mass values are speculative minima based primarily on measurements of lunar rocks.

1219

1220 **Table 8. Estimated spatial resolution achievable by MIXS-T in M1 and X1 flares to make "useful**
1221 **scientific measurements" as defined in Table 7.**

1222

1223 **Table 9. Predicted number of counts for major elemental lines detected by MIXS-C in 1 year of**
1224 **operations.**

1225

1225

	Element % mass						
Model	**Na**	**Mg**	**Al**	**Si**	**Ca**	**Ti**	**Fe**
Chondritic formation[1]	0.03	20	3.4	22	3.7	0.2	5.8
Equilibrium condensation (EC)[2]		24	5.1	19	6.1	0.29	0.078
EC with usage of feeding zones[2]		25	3.8	21	4.7	0.22	0.06
Dynamically mixed[2]		29	2.5	20	2.9	0	0
Collisionally differentiated[2]		33	0	20	1.3	0	0
Vapourisation[3]		25	9	12	4.1	0.5	0.62
Refractory-rich[4]	0	21	8.8	15	11	0.43	0
Intermediate prefered[4]	0.074 - 0.37	19 - 22.9	1.9 - 3.7	16 - 22.4	2.5-5.0	0.090 - 0.18	0.78 - 7.8
Volatile-rich[4]	0.5	19	1.7	21	2.2	0.084	23.4

1226
1227 **Table 1**

1228

1228 **Table 2:**

Element	X-ray Energies and emission lines(keV)	Anorthosite	Troctolite	Low-K Fra Mauro basalt	Medium-K Fra Mauro basalt	Apollo 15 green glass	Apollo 15 Quartz basalt	High-K Apollo 11 basalt
Si	1.74 (K)	20.7	20.5	21.8	22.5	21.4	22.9	19.0
Ti	4.51 (K)	0.04	0.10	0.7	1.3	0.17	0.9	7.1
Al	1.49 (K)	18.6	12.0	10.0	9.3	4.04	4.9	4.6
Fe	0.71 (L) 6.40 (Kα) 7.07 (Kβ)	0.52	3.81	7.5	8.5	15.3	14.5	14.8
Mn	5.91 (K)	0	0.05	0.0	0.0	0.16	0.2	0.2
Mg	1.25 (K)	0.48	8.86	6.6	5.2	10.0	5.7	4.6
Ca	3.70(Kα) 4.02(Kβ)	13.4	9.36	8.3	7.6	6.23	7.7	7.3
Na	1.04 (K)	0.59	0.29	0.3	0.5	0.09	0.2	0.4
K	3.35 (K)	0	0.00	0.2	0.7	0.03	0.0	0.4
P	2.02 (K)	0	0.00	0.0	0.0	0.00	0.0	0.1
Cr	5.41 (Kα) 5.95 (Kβ)	0	0.07	0.2	0.1	0.34	0.5	0.3
Ni	7.47 (Kα)	0	0.03	0.2	0.37		0.01	0.002

1229
1230

1230 Table 3:

Element	Line	Quiet Sun	B1 Flare	C1 Flare	M1 Flare
O	K	0.04	0.05	0.08	0.007
Na	K	66	64	20	2.0
Mg	K	14	8.2	1.9	0.23
Al	K	58	17	3.2	0.42
Si	K	53	7.2	1.1	0.16
P	K	$2.1x10^{7}$	$1.1x10^{5}$	2000	170
K	K		$2.5x10^{5}$	270	61
Ca	Kα	$3.2x10^{6}$	3900	18	4.3
Ca	Kβ		$2.3x10^{5}$	140	32
Ti	Kα		$2.57x10^{5}$	58	12
Ti	Kβ		$1.55x10^{7}$	440	93
Cr	Kα			$4.3x10^{4}$	980
Cr	Kβ			$2.3x10^{6}$	$6.1x10^{4}$
Fe	Kα		$1.5x10^{7}$	440	40
Fe	Kβ			$2.2x10^{4}$	300
Fe	Lα	0.46	0.68	0.51	0.05
Fe	Lβ	0.50	0.74	0.53	0.05
Ni	Lα	$3.9x10^{5}$	$5.0x10^{5}$	$1.9x10^{5}$	$1.8x10^{4}$
Ni	Lβ	$4.3x10^{5}$	$5.5x10^{5}$	$2.0x10^{5}$	$1.9x10^{4}$

1231
1232

1232 Table 4:

Element	Line	Quiet Sun	B1 Flare	C1 Flare	M1 Flare
O	K	0.01	0.01	0.02	0.0018
Na	K	13	12	3.8	0.42
Mg	K	2.7	1.53	0.36	0.04
Al	K	10	3.05	0.57	0.07
Si	K	8.4	1.15	0.17	0.03
P	K	$1.3x10^5$	960	80	13
K	K	$1.9x10^6$	1600	21	4.8
Ca	Kα	$1.5x10^4$	110	1.2	0.29
Ca	Kβ	$7.1x10^5$	900	8.5	2.0
Ti	Kα	$1.8x10^5$	750	3.1	0.66
Ti	Kβ	$8.1x10^6$	$3.4x10^4$	21	4.4
Cr	Kα		$5.1x10^6$	200	29
Cr	Kβ			3700	200
Fe	Kα	$2.6x10^6$	$1.5x10^4$	14	1.3
Fe	Kβ		$7.2x10^5$	95	8.6
Fe	Lα	0.09	0.13	0.09	0.01
Fe	Lβ	0.10	0.14	0.10	0.01
Ni	Kα				$1.2x10^6$
Ni	Lα	$6.6x10^4$	$8.2x10^4$	$3.3x10^4$	3400
Ni	Lβ	$7.2x10^4$	$8.9x10^4$	$3.4x10^4$	3600

1233
1234

1234 Table 5:

Element	Line	Number of counts	% error
O	K	$1.3x10^4$	0.6
Na	K	14	30
Mg	K	70	10
Al	K	17	20
Si	K	19	20
Fe	Lα	1500	2
Fe	Lβ	1500	2

1235
1236

1236 Table 6:

Element	Line	Number of counts	% error
O	K	$6.1x10^6$	0.03
Na	K	6500	1
Mg	K	$3.4x10^4$	0.5
Al	K	8700	1
Si	K	$1.1x10^4$	1
Fe	Lα	$7.6x10^5$	0.1
Fe	Lβ	$6.6x10^5$	0.1

1237
1238

1238 Table 7:

Element	Possible minimum % mass	Minimum Precision required (%)
Si	20	5
Ti	1	20
Al	1	20
Fe	2	50
Mg	2	25
Ca	18	20
Na	0.4	Detection
K	0.1	Detection
Cr	0.05	Detection
Ni	0.04	Detection
S	0.1 (at poles)	Detection

1239
1240

1240 Table 8:

Flare State	**X1**	**M1**
Element	Spatial resolution (km)	Spatial resolution (km)
Na	3	9
Mg	1	4
Al	2	6
Si	5	15
P	25	
K	15	
Ca	6	20
Ti	10	
Fe	1	1

1241
1242

1242 Table 9:

Element	Line	Counts	error (%)
O	K	$7.6x10^9$	0.00081
Na	K	$8.0x10^6$	0.034
Mg	K	$4.2x10^7$	0.015
Al	K	$1.1x10^7$	0.031
Si	K	$1.3x10^7$	0.027
P	K	12000	0.91
K	K	3200	1.77
Ca	Kα	37000	0.52
Ca	Kβ	5400	1.38
Ti	Kα	10000	0.96
Fe	Kα	3000	1.8
Fe	Lα	$9.0x10^8$	0.0028
Fe	Lβ	$5.7x10^8$	0.0029
Ni	Lα	98000	0.32
Ni	Lβ	90000	0.33

1243
1244

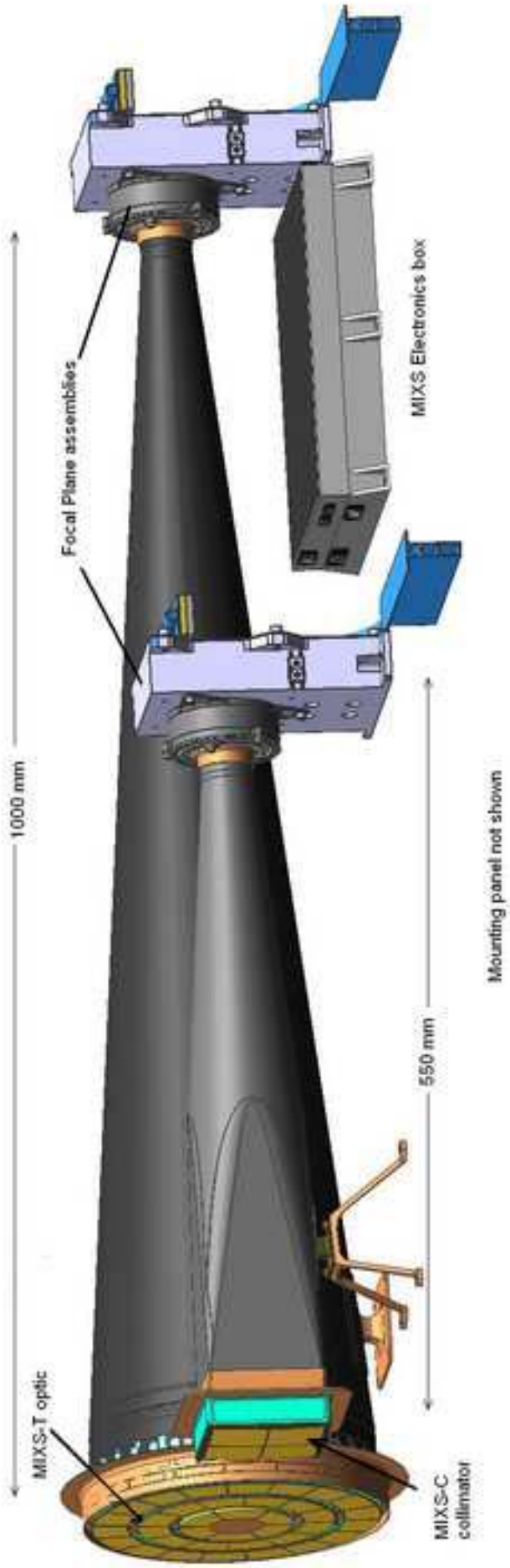

Figure 1

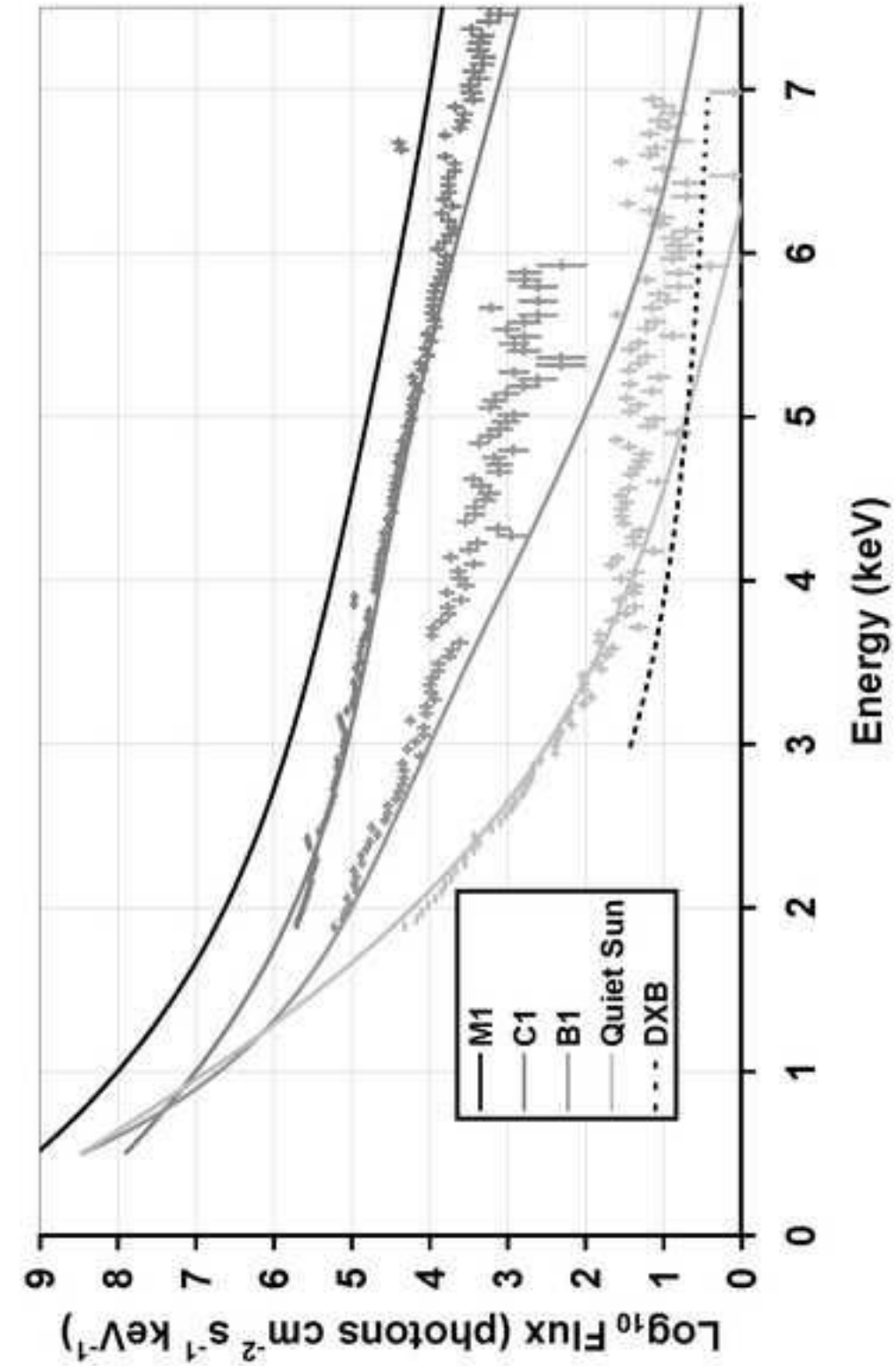
Log10 Flux (photons cm-2 s-1 keV-1)
Energy (keV)
0
1
2
3
4
5
6
7
8
9
M1
C1
B1
Quiet Sun
DXB

Figure2

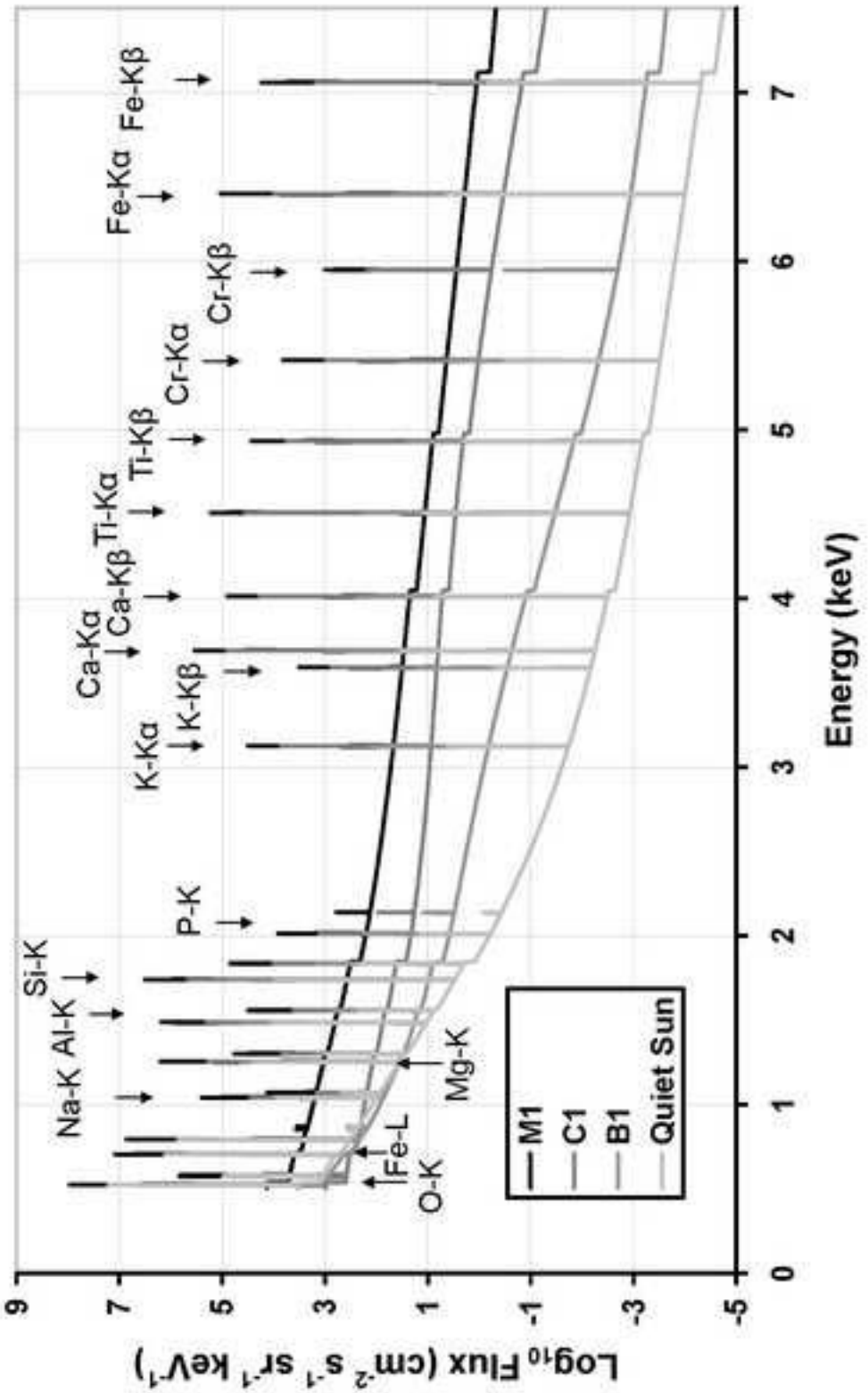
Log10 Flux (cm-2 s-1 sr-1 keV-1)
Energy (keV)
9
7
5
3
1
-1
-3
-5
0
1
2
3
4
5
6
7
Si-K
Na-K
Al-K
P-K
K-Kα
K-Kβ
Ca-Kα
Ca-Kβ
Ti-Kα
Ti-Kβ
Cr-Kα
Cr-Kβ
Fe-Kα
Fe-Kβ
Fe-L
O-K
Mg-K
M1
C1
B1
Quiet Sun

Figure3

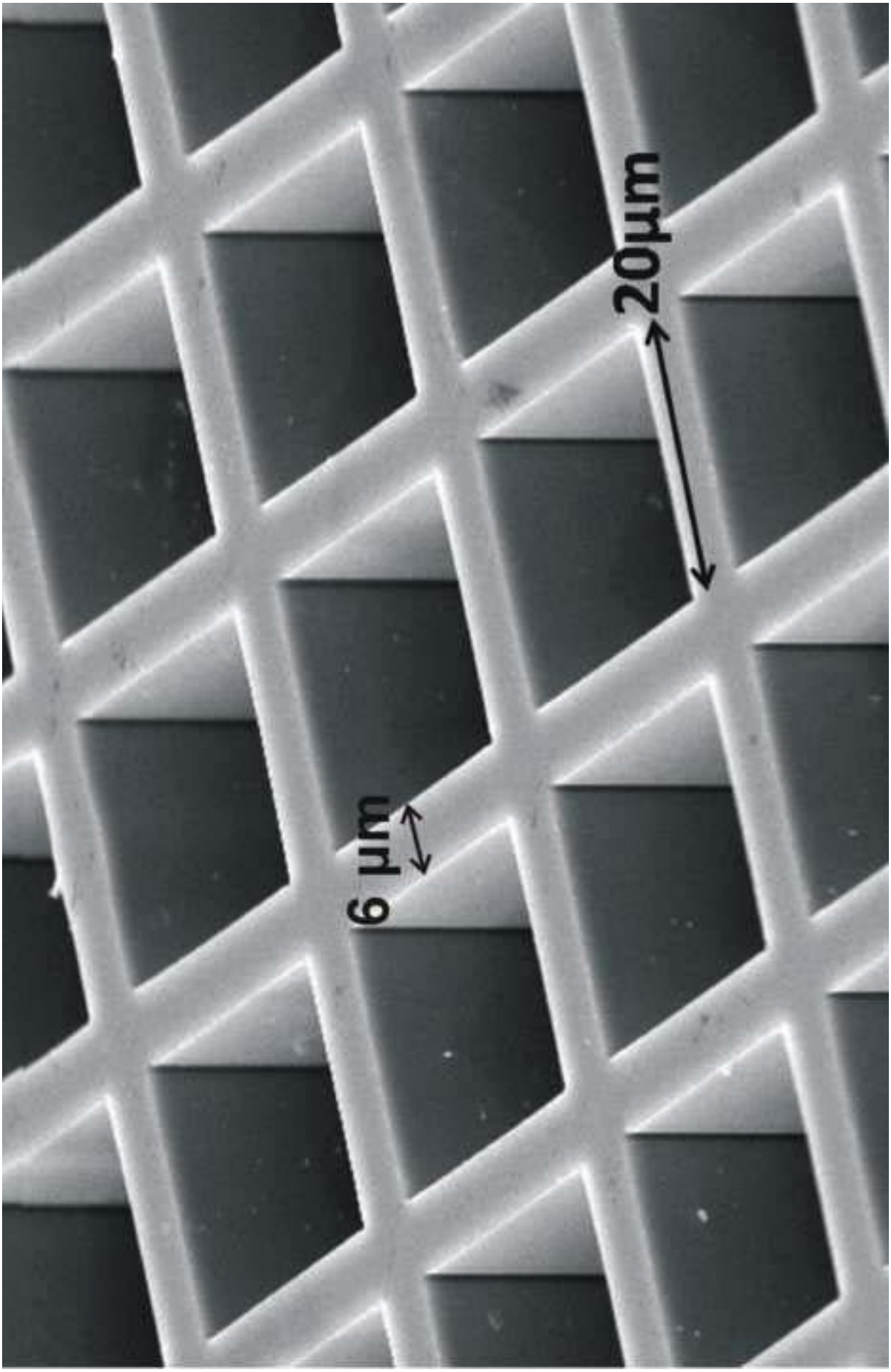

Figure 4

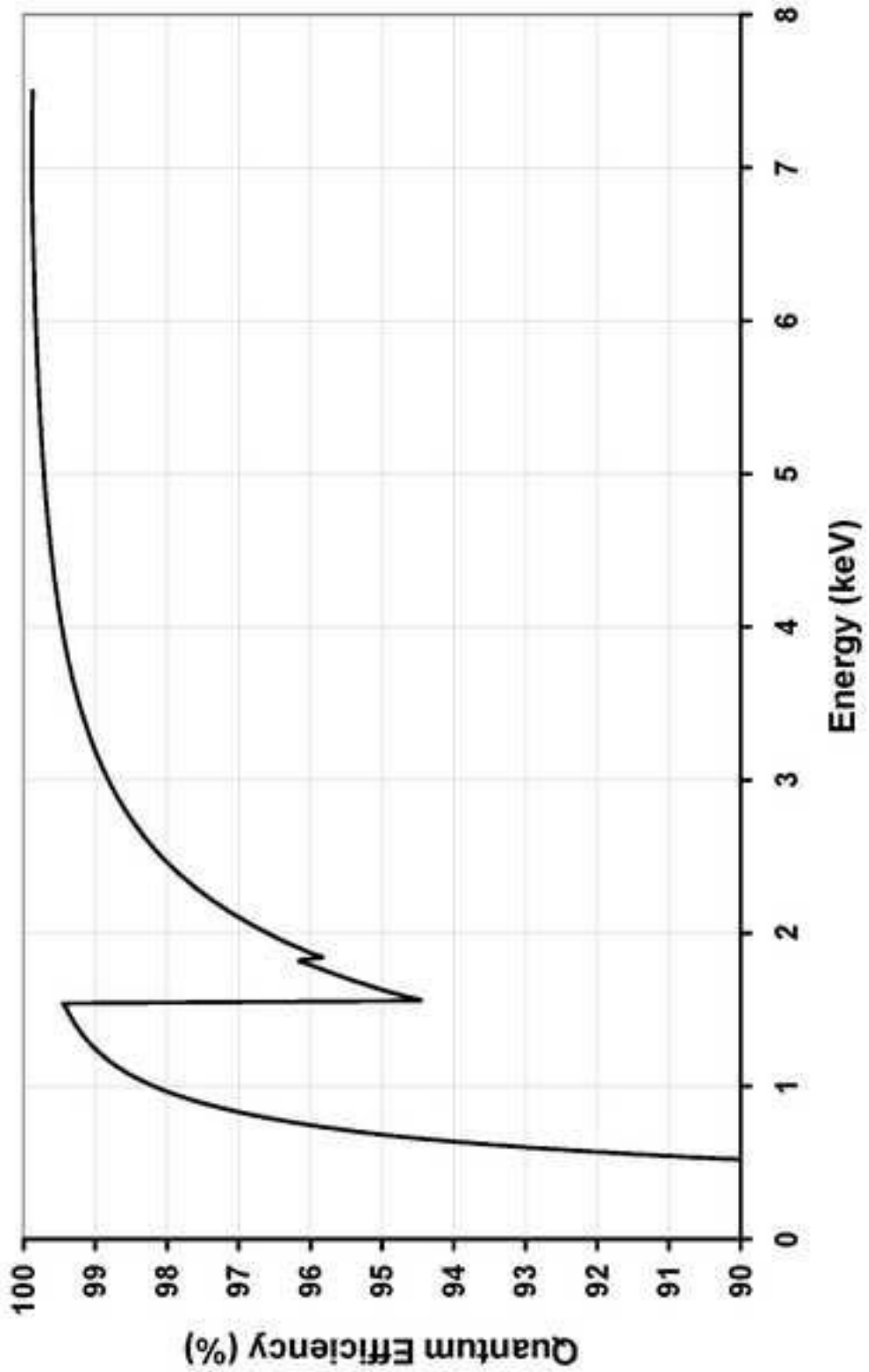
Quantum Efficiency (%)
100
99
98
97
96
95
94
93
92
91
90
0
1
2
3
4
5
6
7
8
Energy (keV)

Figure5

Figure6

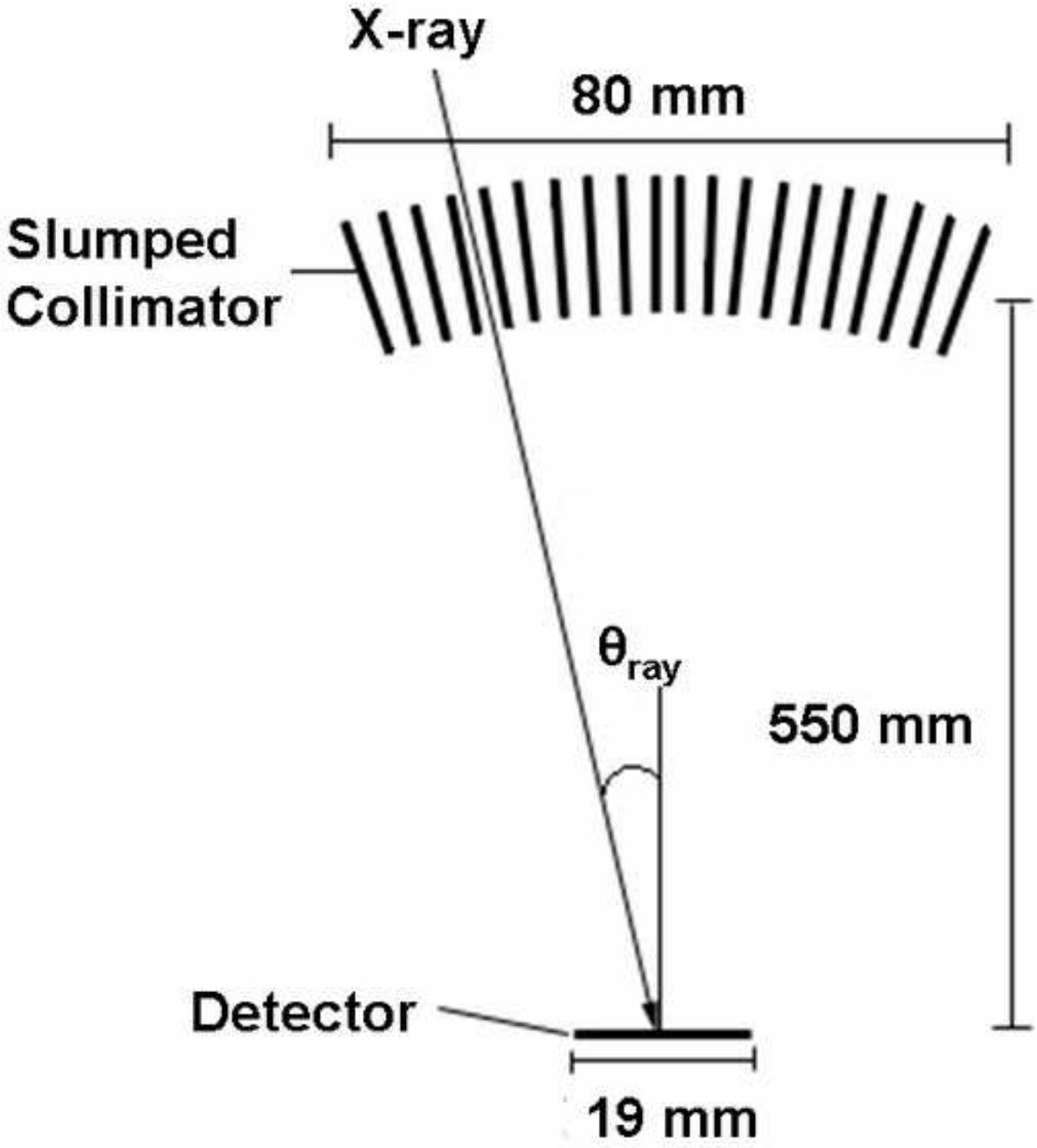

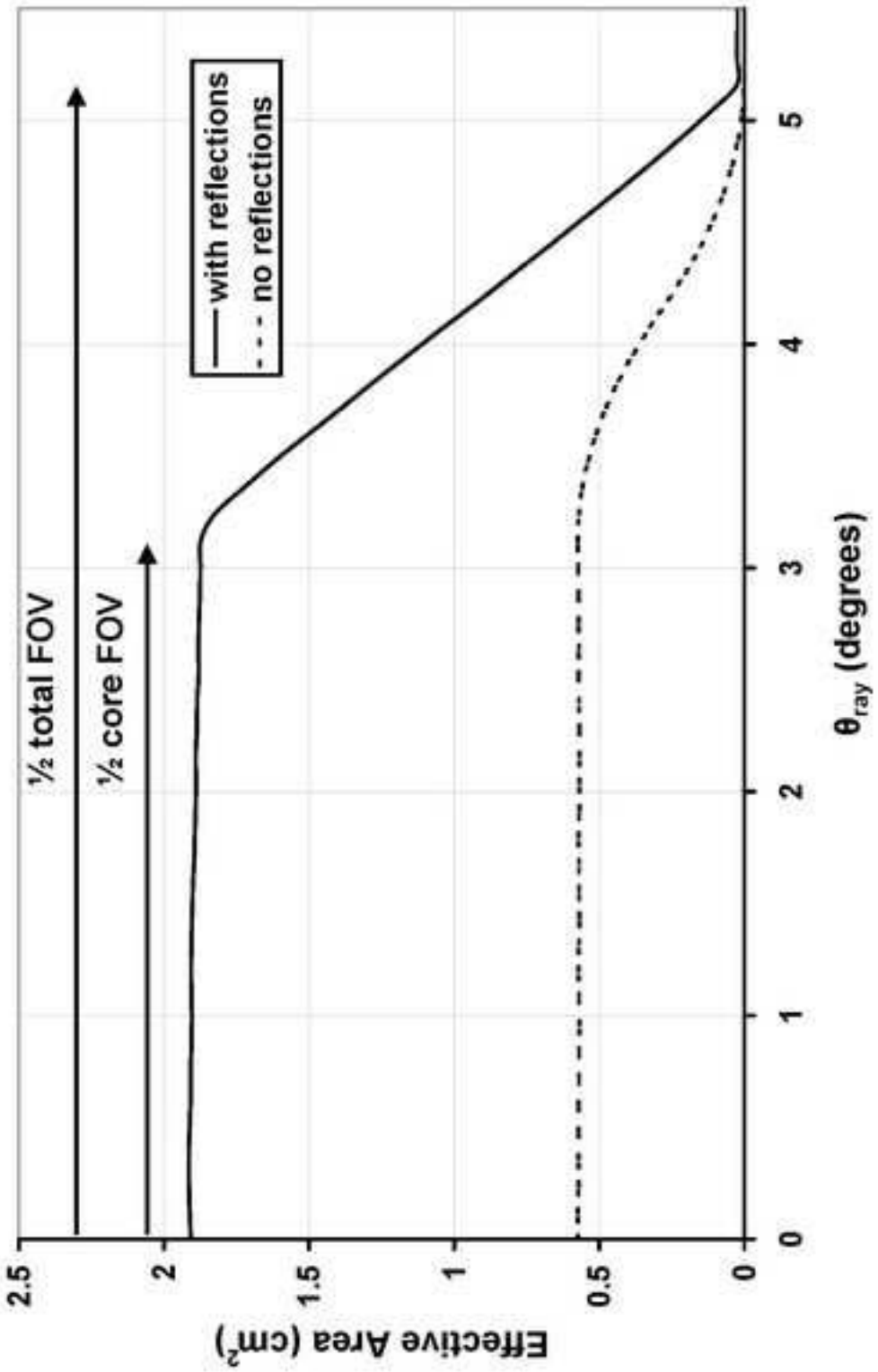
with reflections
no reflections
½ total FOV
½ core FOV
Effective Area (cm²)
θray (degrees)
0
0.5
1
1.5
2
2.5
0
1
2
3
4
5

Figure7

Figure8

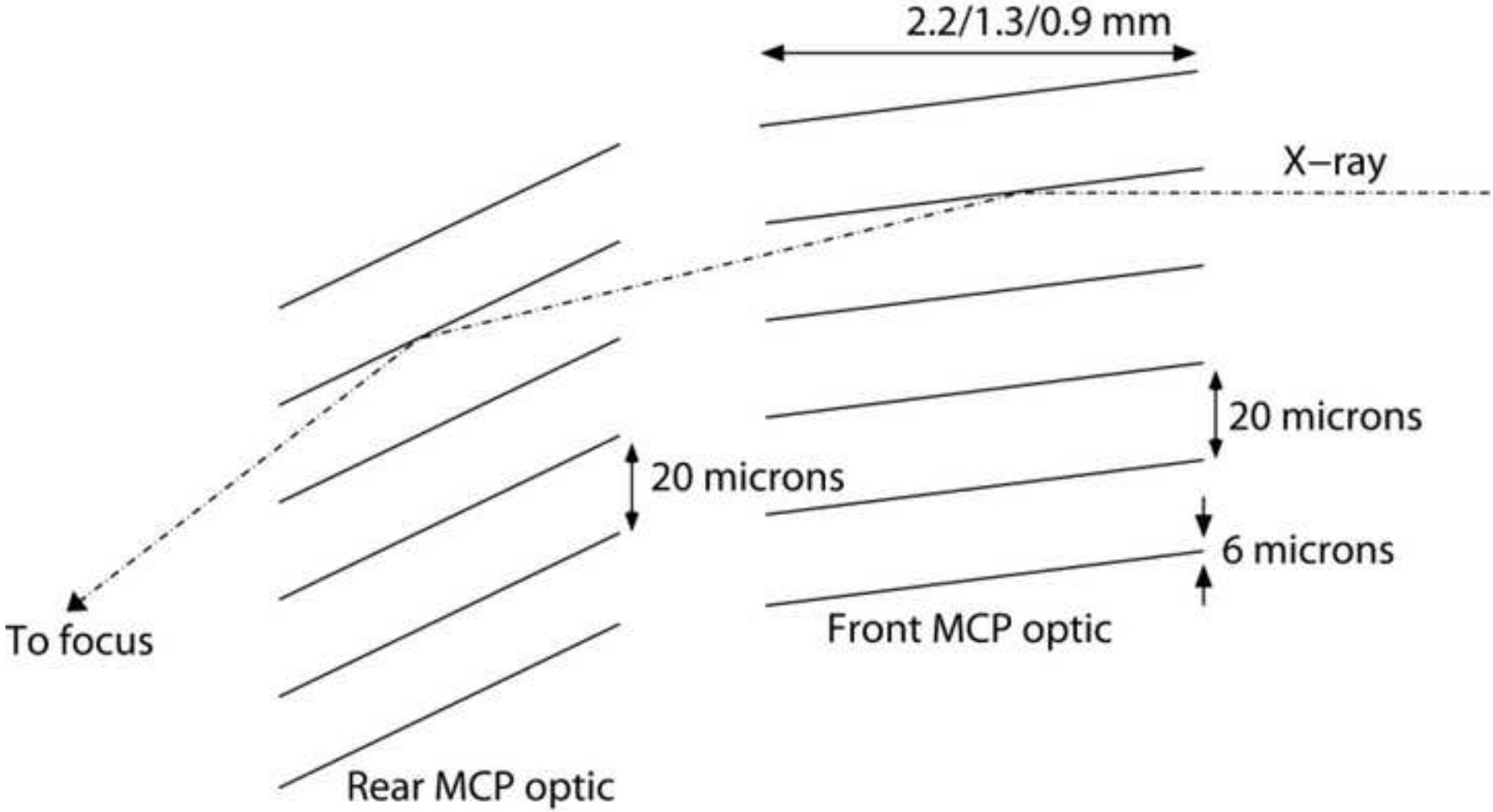

Figure9

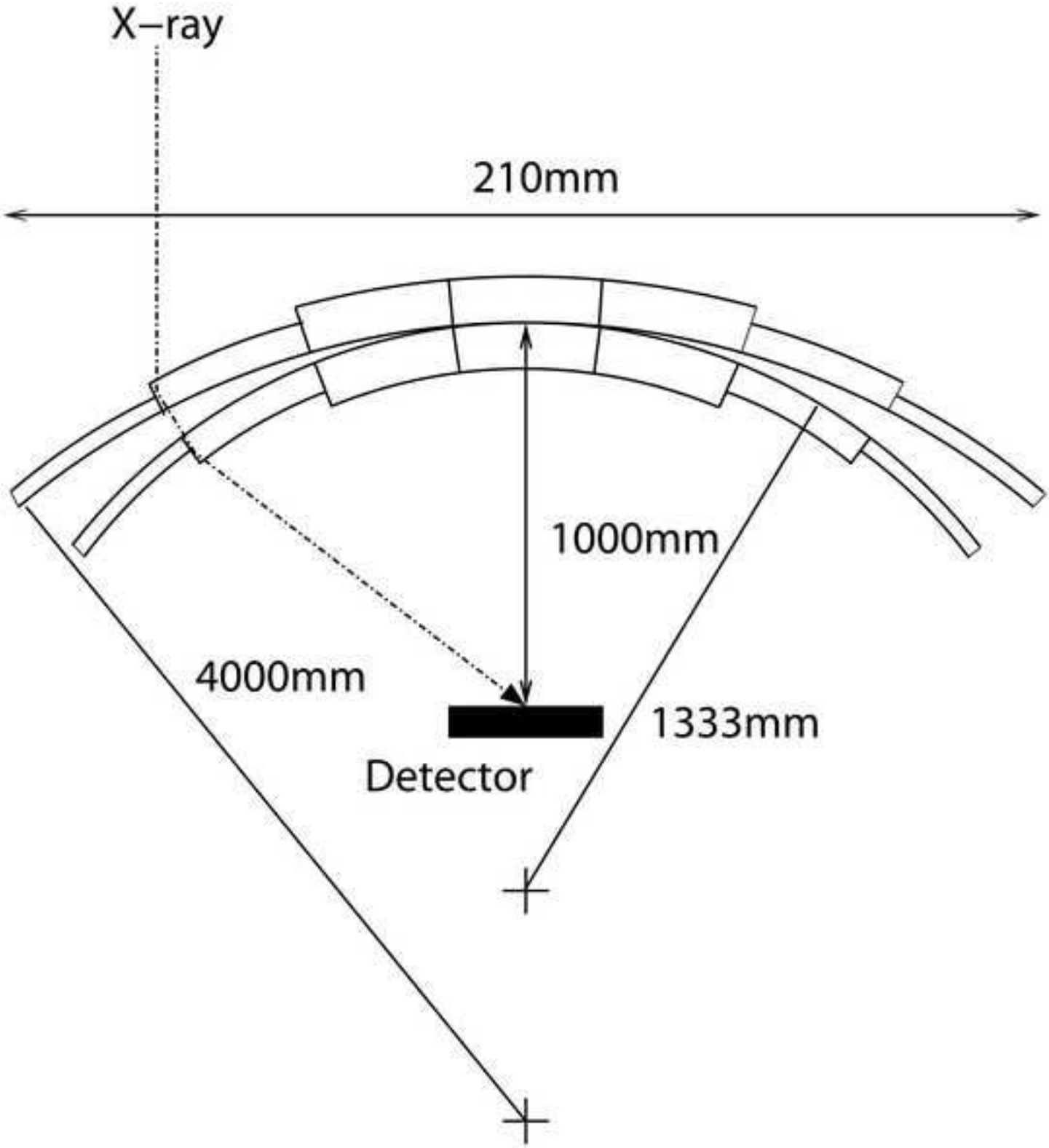

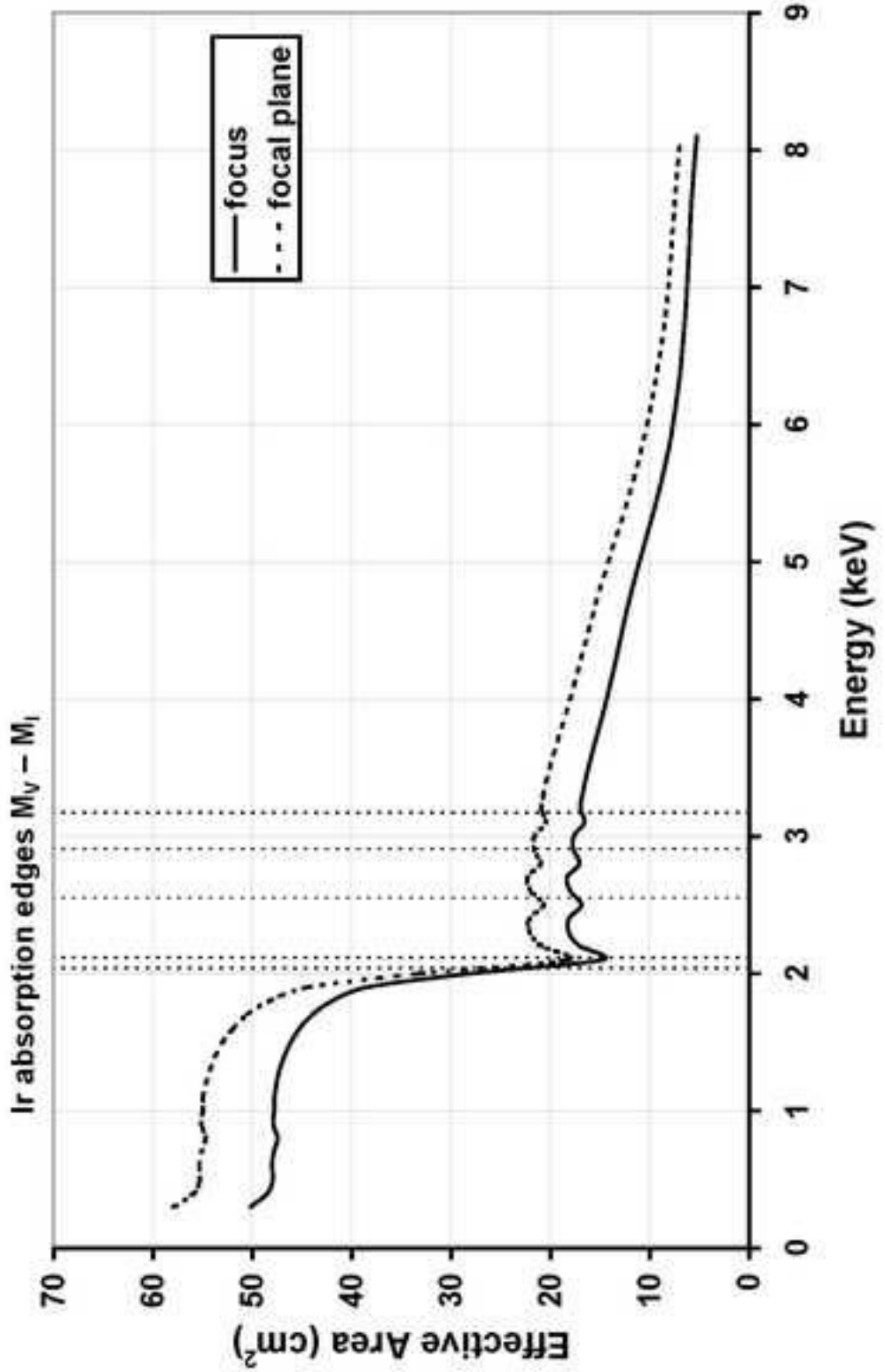
focus
focal plane
Ir absorption edges $M_V - M_I$
Effective Area (cm^2)
Energy (keV)
0
10
20
30
40
50
60
70
0
1
2
3
4
5
6
7
8
9

Figure10

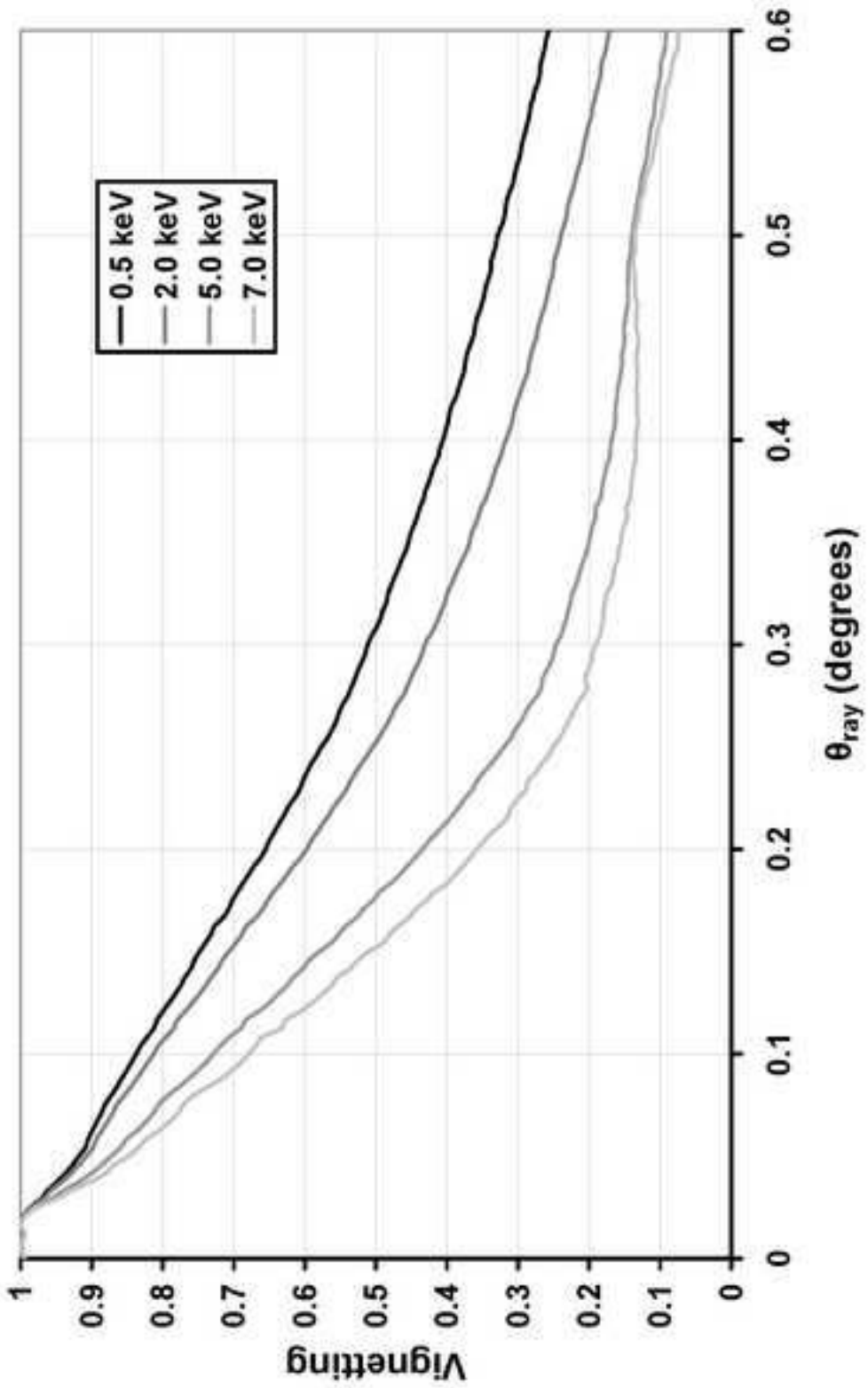
0.5 keV
2.0 keV
5.0 keV
7.0 keV
Vignetting
1
0.9
0.8
0.7
0.6
0.5
0.4
0.3
0.2
0.1
0
0
0.1
0.2
0.3
0.4
0.5
0.6
θray (degrees)

Figure11

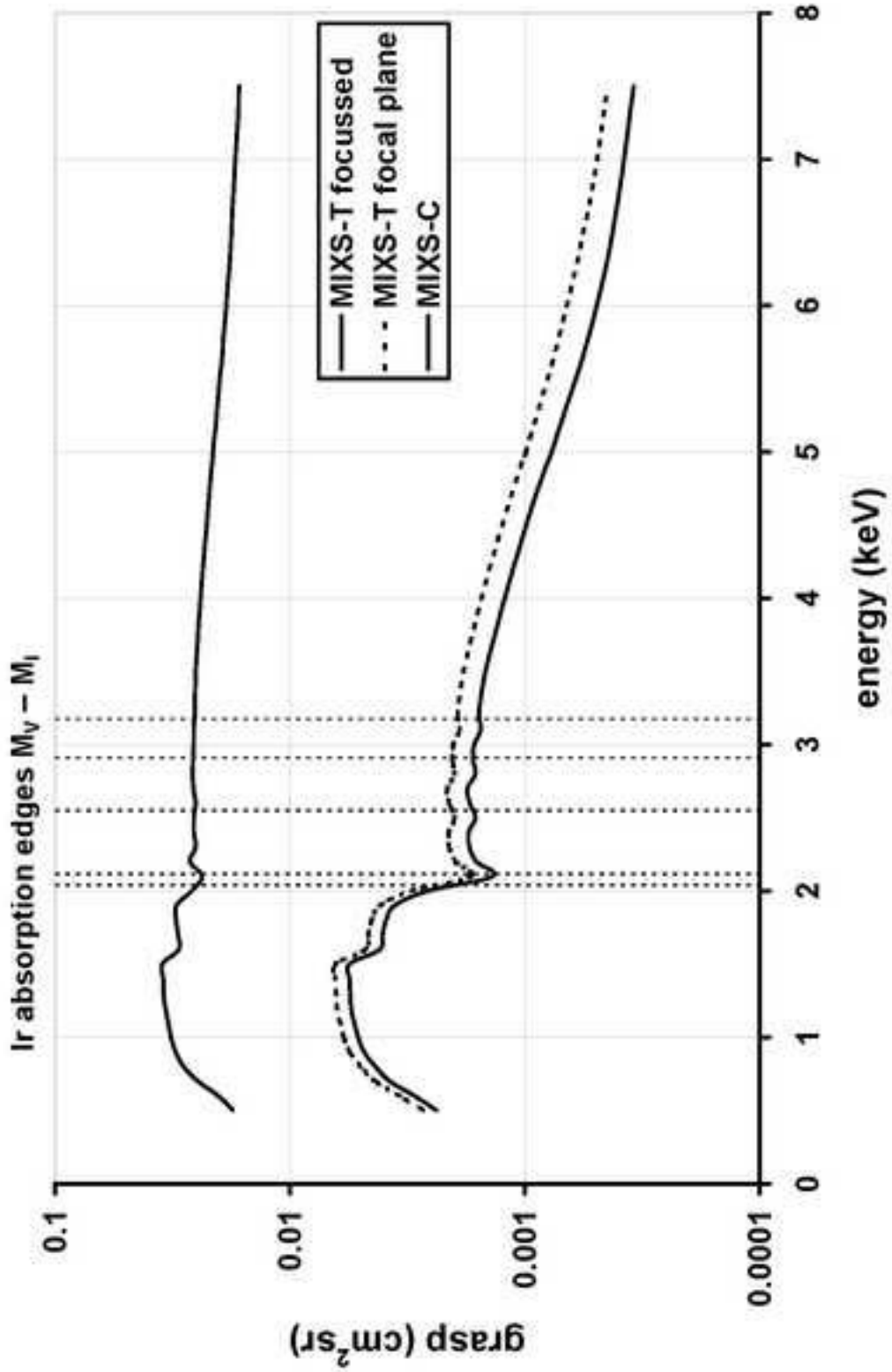
MIXS-T focussed
MIXS-T focal plane
MIXS-C
Ir absorption edges $M_V - M_I$
grasp (cm²sr)
0.1
0.01
0.001
0.0001
0
1
2
3
4
5
6
7
8
energy (keV)

Figure12

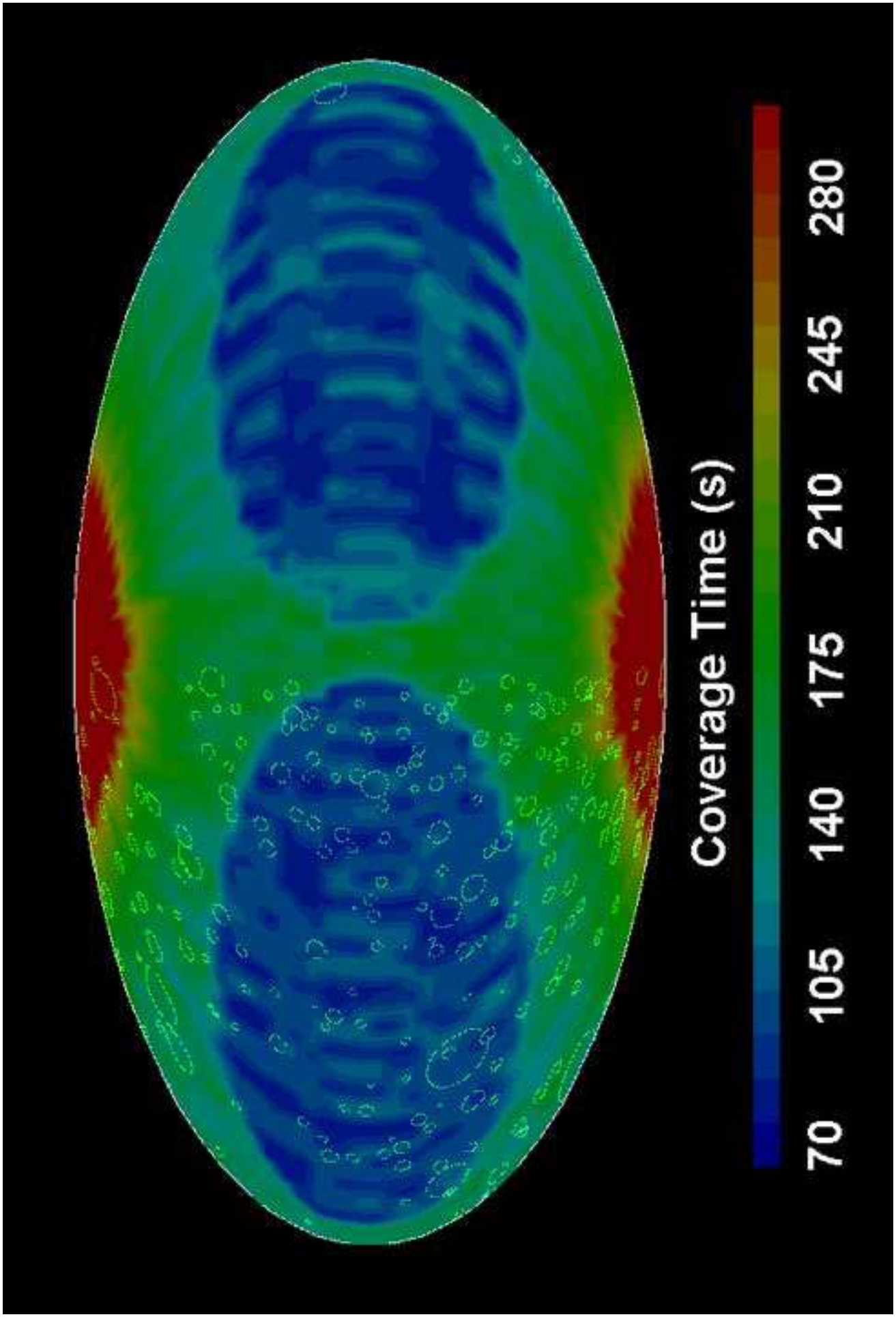

Figure13

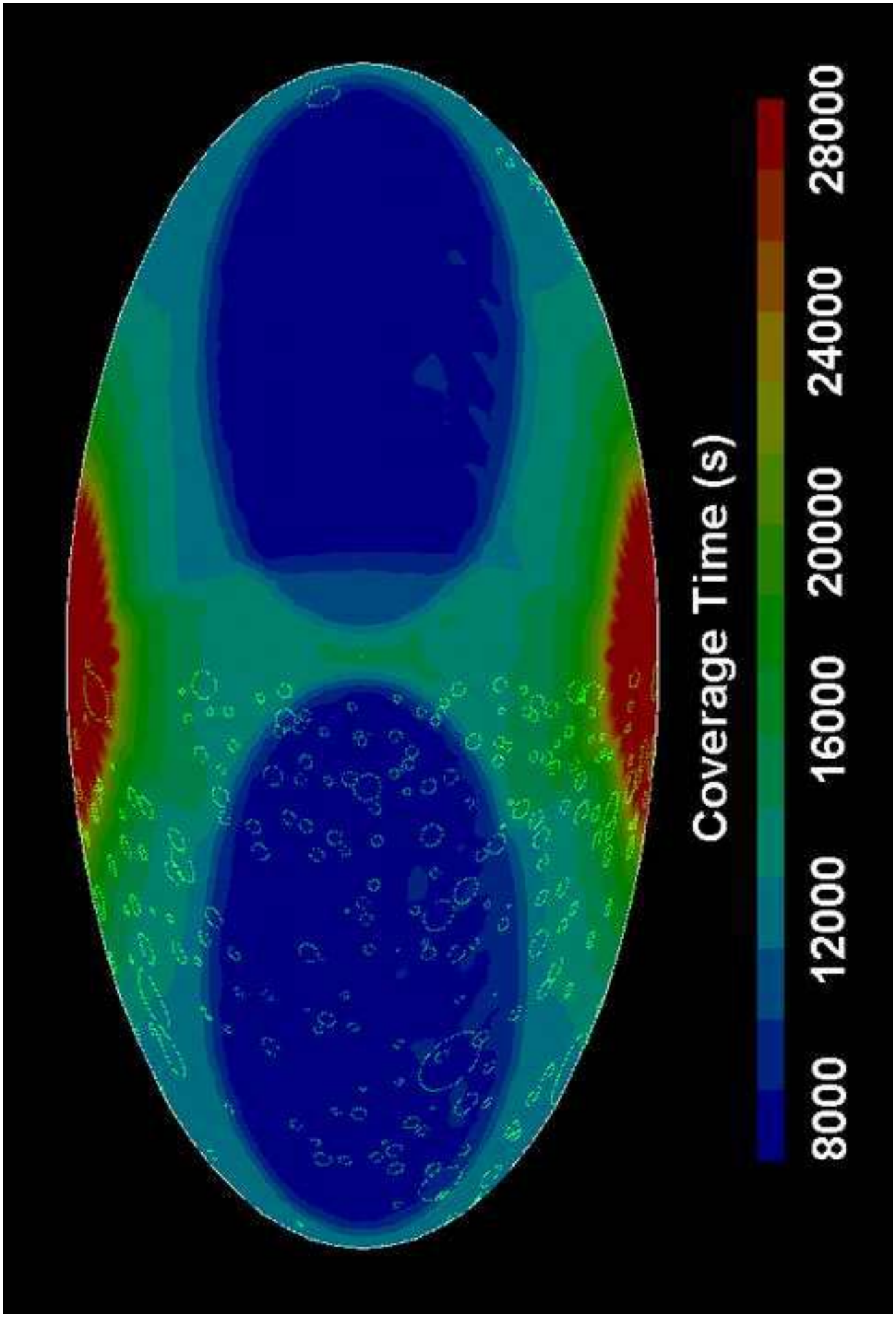

Figure14

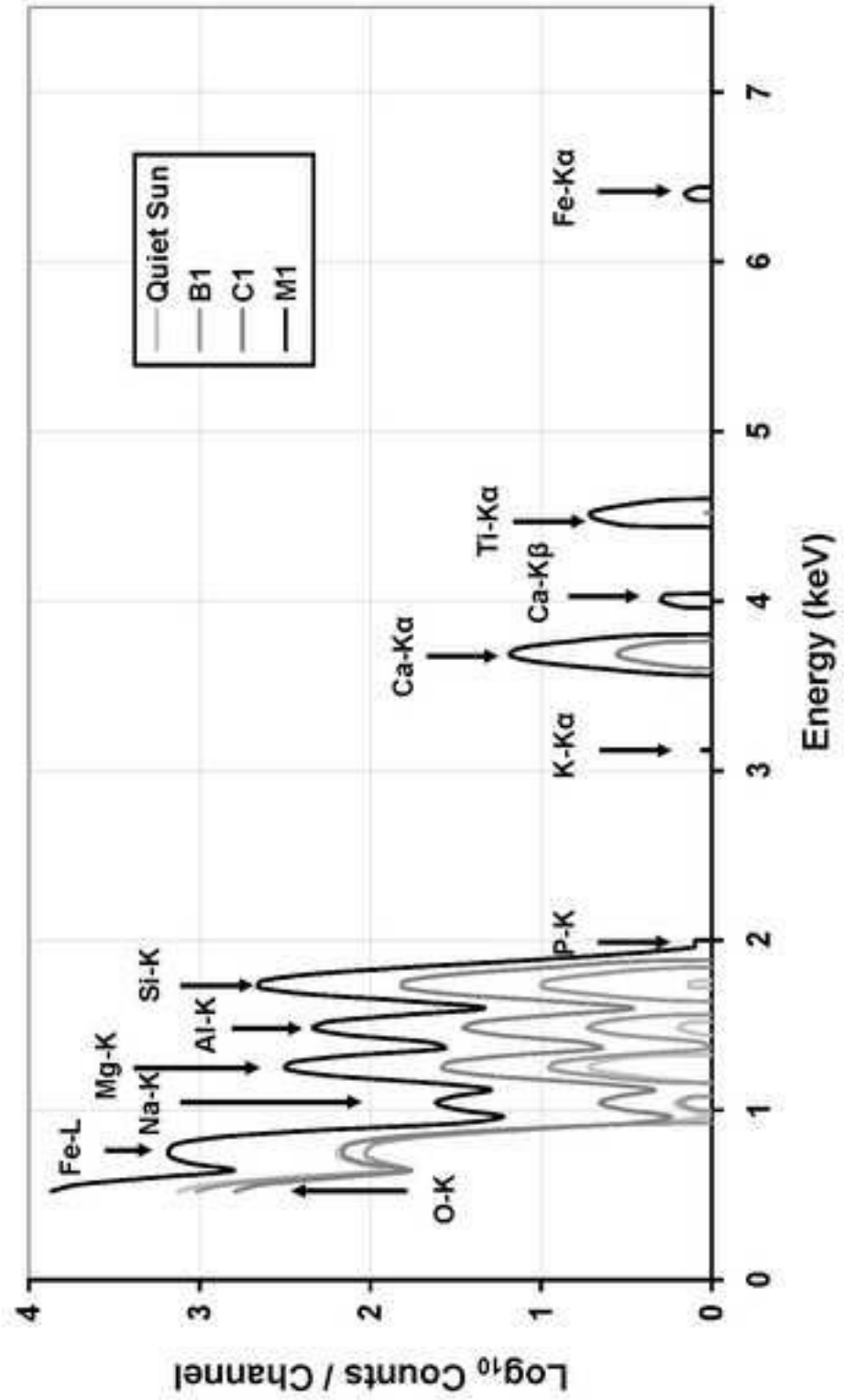
Log10 Counts / Channel
Energy (keV)
Quiet Sun
B1
C1
M1
Fe-L
Mg-K
Na-K
Al-K
Si-K
O-K
P-K
K-Kα
Ca-Kα
Ca-Kβ
Ti-Kα
Fe-Kα
0
1
2
3
4
5
6
7

Figure15

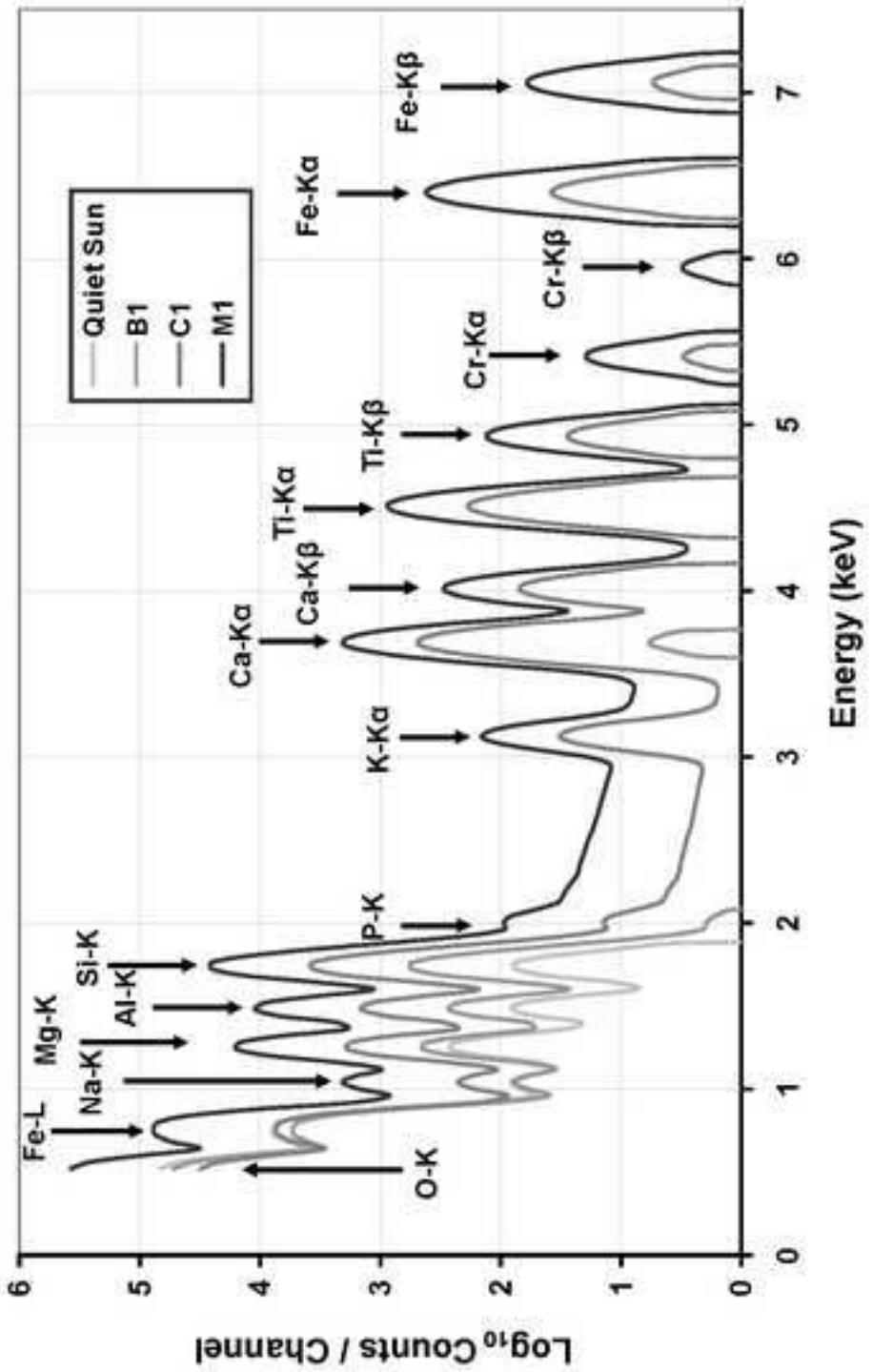
Quiet Sun
B1
C1
M1
Fe-L
Na-K
Mg-K
Al-K
Si-K
P-K
K-Kα
Ca-Kα
Ca-Kβ
Ti-Kα
Ti-Kβ
Cr-Kα
Cr-Kβ
Fe-Kα
Fe-Kβ
O-K
Log10 Counts / Channel
Energy (keV)
0
1
2
3
4
5
6
7

Figure16

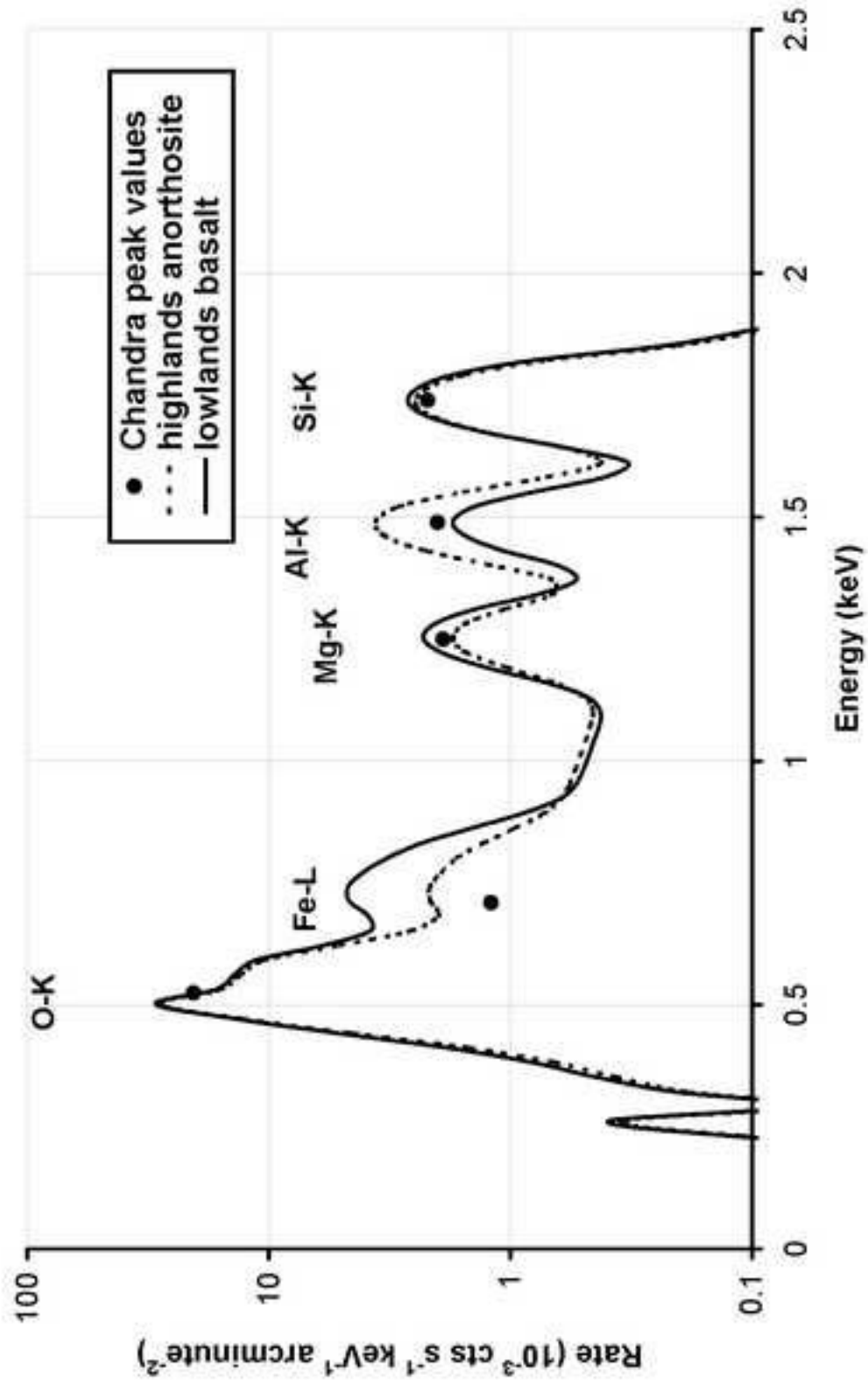
Chandra peak values
highlands anorthosite
lowlands basalt
O-K
Fe-L
Mg-K
Al-K
Si-K
100
10
1
0.1
0
0.5
1
1.5
2
2.5
Energy (keV)
Rate (10-3 cts s-1 keV-1 arcminute-2)

Figure17